ZIRAT 24 STR
Mechanical Properties of Reactor Core Materials

Authors

Kit Coleman
Deep River, ON, Canada

Tahir Mahmood
Pleasanton, CA, USA

Clément Lemaignan
Voreppe, France

Malcolm Griffiths
Deep River, ON, Canada

A.N.T. INTERNATIONAL®

Advanced Nuclear Technology International
Analysvägen 5, SE-43533 Mölnlycke
Sweden

info@antinternational.com
www.antinternational.com

Ecolabelled printed matter, 441 799

Disclaimer

The information presented in this report has been compiled and analysed by Advanced Nuclear Technology International Europe AB (ANT International®) and its subcontractors. ANT International has exercised due diligence in this work, but does not warrant the accuracy or completeness of the information. ANT International does not assume any responsibility for any consequences as a result of the use of the information for any party, except a warranty for reasonable technical skill, which is limited to the amount paid for this report.

Quality-checked and authorized by:

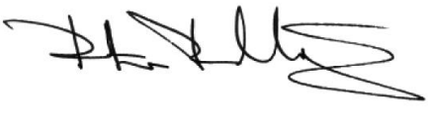

Mr Peter Rudling, President of ANT International

Contents

1 Mechanical Properties of Reactor Core Materials

1.1 Introduction

In materials science, the strength of a material is its ability to withstand an applied stress without failure. Yield strength refers to the point beyond which the material deforms plastically, i.e. the point at which the deformation cannot be reversed upon removal of the loading. The ultimate strength refers to where the maximum load cannot be sustained with further plastic deformation. The applied stress may be tensile, compressive, or shear. For a simple tensile test, the engineering stress, σ_E, is defined as the load divided by the initial cross-sectional area of the specimen, A_0, and the engineering strain, ε_E, is defined as the change in length divided by the original length of the specimen. An idealised engineering stress-strain curve (for a single crystal) is shown in Figure 1-1(a) and the development of specimen shape is depicted in Figure 1-1(b). In the elastic region (1) the strain is a function of Young's modulus, E, through σ/E. The point where the stress-strain curves deviates from linearity is the proportional limit (2). The material may still deform elastically (recoverable) up to a point known as the elastic limit (3). Often the point at which the material starts to deform plastically is difficult to define. For this reason, engineers use a measure for the yield strength known as the 0.2% offset yield strength (4) that is the stress evaluated after 0.2% plastic strain.

Often the stress-strain curves for engineering materials are not as simple as that portrayed in Figure 1-1. There may be a load drop (softening) due to the unpinning of dislocations or twinning or, in the case of irradiated materials, clearing of irradiation damage. This softening gives rise to an upper and lower yield point (Figure 1-2). Some studies associate this upper and lower yield behaviour with strain-aging when the lower yield is followed by jerky flow. In strain-aging the yield occurs when dislocations that are pinned by solute atoms exceed the pinning stress and advance until they are stopped as they encounter further barriers to slip. Once stopped, solute atoms can migrate to the dislocations thus pinning them again and adding to the friction stress that must be exceeded before dislocation slip can proceed further. A repeating cycle gives rise to the characteristic jerky flow associated with strain aging. Such jerky flow is also a result of twinning, which also has to be considered when jerky flow is observed. Strain aging is discussed further in section 2.1. For the most part strain-aging does not significantly affect the stress-strain behaviour of irradiated materials because other factors (irradiation hardening and strain localisation) appear to be more dominant.

The engineering stress-strain curve for a typical engineering component is shown as the red curve in Figure 1-2. Yielding is most often associated with the creation and motion of dislocations. The plastic strain, ε_p, is a function of the dislocation density, ρ, and the distance, ℓ, travelled by the dislocations with Burgers vector, b, and $\varepsilon_p = \rho b \ell$. As deformation progresses the dislocations may become entangled or piled-up at boundaries and the material exhibits work-hardening. The stress increases as the load is increased to maintain the deformation of the hardened material. For a given load, the true stress of the material also increases as it elongates because the cross-sectional area is reduced. The true stress and strain of the material is shown by the blue curve in Figure 1-2. A tensile specimen may deform uniformly up to the point where the material can no longer sustain the load (the ultimate tensile strength). At this point localised deformation (necking) may occur and, although the material may still be work-hardening in the necked region, i.e. increasing in strength locally, the load can no longer be supported, the engineering stress decreases until the point of rupture (point 3 in Figure 1-2).

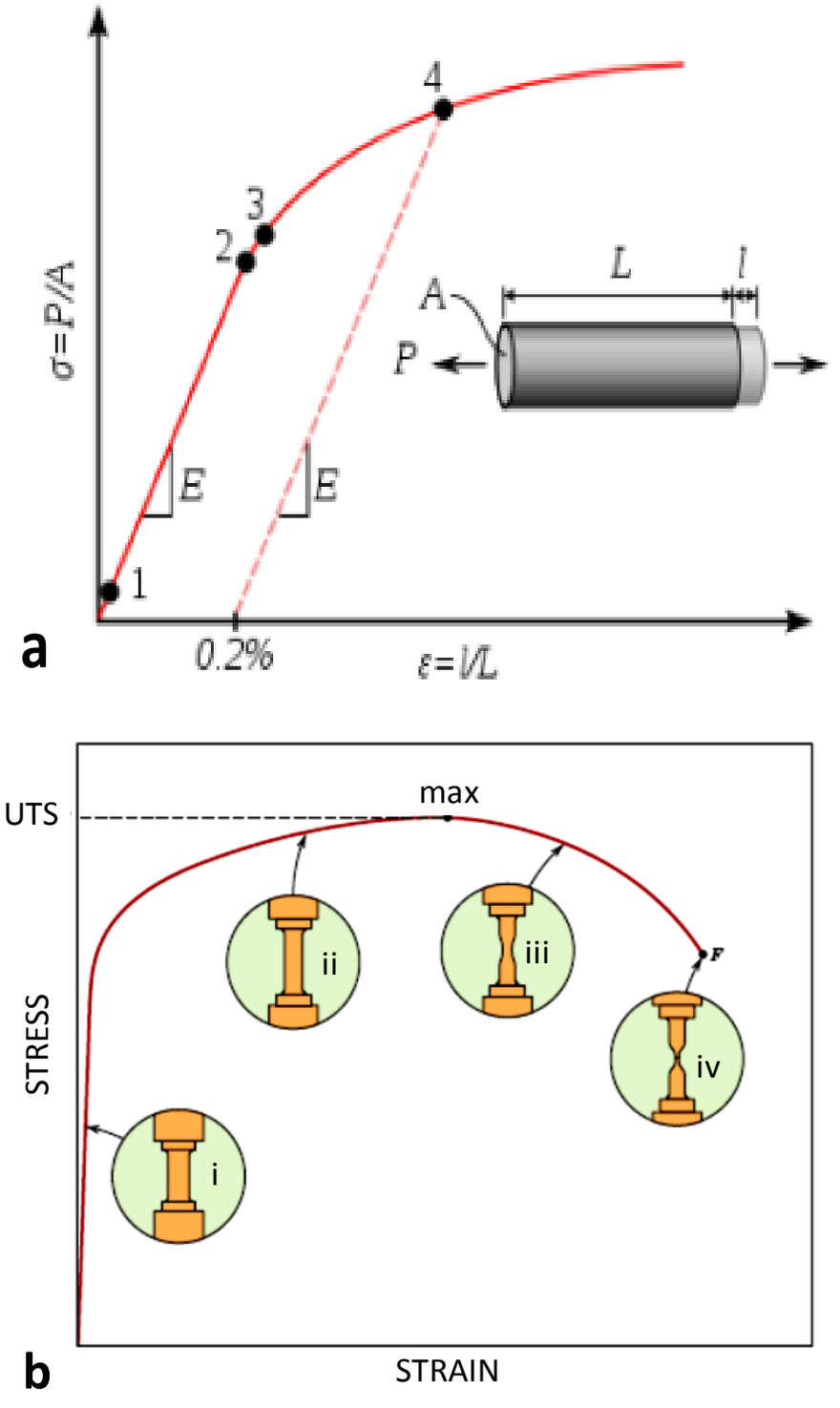

Figure 1-1: (a) Stress–strain curve showing typical yield behaviour for non-ferrous alloys. Stress (σ) is shown as a function of strain (ε) and is given by E.ε (1). Different stages of the stress-strain curve are shown: proportional limit (2); true elastic limit (3); 0.2% offset yield strength (4); (b) stress stain curve showing ultimate tensile strength (UTS) and the dimensional changes in tensile specimens showing in order: (i) elastic strain; (ii) uniform elongation; (iii) necking; (iv) failure.

2 Mechanical Properties of:

2.1 Zirconium alloys: Uniaxial tensile ductility below 500 °C

2.1.1 Introduction

Uniaxial tensile testing of zirconium alloys has many uses: to confirm that the material meets a specification, to evaluate new alloys or old ones modified by changes in fabrication, to assess the effects of reactor operation and to elucidate mechanisms of strengthening or embrittlement. Often a standard test method is used, for example, the ASTM Methods E 8 [ASTM, 2009a] and E 21 [ASTM, 2009b]. The outcomes are measurements of strength such as 0.2% yield strength and UTS, and measurements of ductility, such as uniform and total elongation, and reduction in area at fracture. This section will be mostly concerned with the phenomenology of hardening and tensile ductility.

Without intervention by other mechanisms, such as stress corrosion cracking, zirconium alloys fracture in a ductile manner when specimens or components are highly stressed in tension. During normal reactor operation, failure of components by ductile fracture is unlikely because large safety margins are included by design. For load bearing structures the specification requires that the material has a certain strength that is several times that of the design stress. For example, pressure-retaining components may follow the principles of Section III of the American Society of Mechanical Engineers (ASME) Boiler and Pressure Vessel Code; at the maximum operating temperature the imposed stress must not exceed the lowest of:

- 1/3 of the ultimate tensile strength (UTS),
- 2/3 of the yield strength,
- 3/5 of the stress to produce rupture within 100 000 hours, or
- the stress to provide a creep rate of 10^{-7} per hour.

Figure 2-1 shows schematically the temperature regimes where short-term and long-term mechanical properties of zirconium alloys control the design stress for pressurized tubes. Up to about 350 °C design strength is controlled by short-term tensile properties.

2.1.2 Behaviour of unirradiated material

If cracks initiate and propagate by stable mechanisms, a useful line of defence against rupture is good ductility. Before irradiation, zirconium alloys behave similarly to other ductile metals in a tensile test. In a load-elongation curve, an initial linear elastic rise in load is followed by yielding when the rate of rise in load declines during plastic deformation until a maximum value is reached – the UTS – followed by a gradual decrease in load to fracture. Occasionally test specimens exhibit a definite yield point instead of a gradual deviation from elastic behaviour; for example, in pure zirconium with small grains (< 8 µm) [Keeler, 1955; Coleman & Hardie, 1966e; Weinstein, 1966] or large grains – 910 µm [Ramani & Rodriguez, 1972], in Zircaloy-2 [Lee, 1970] and in Zr-1Nb [Thorpe, 1978]. A rise in load after yield during plastic deformation indicates work-hardening. When elongation rate is varied, strain-rate hardening is also observed. The true flow stress, σ_T,-true strain; ε_T,-true strain-rate; $\dot{\varepsilon}_T$, relationship can be described by several methods. As examples, work hardening may be fitted to power functions [Hollomon, 1945; Ramberg & Osgood, 1943; Swift, 1952] or exponential functions [Voce, 1947]. Including strain rate effects in the power functions leads to [Hollomon, 1946]:

Equation 2-1:

$$\sigma_T = H\ {\varepsilon_T}^h\ {\dot{\varepsilon}_T}^m$$

where H is strength constant

h is work-hardening coefficient

m is strain rate sensitivity

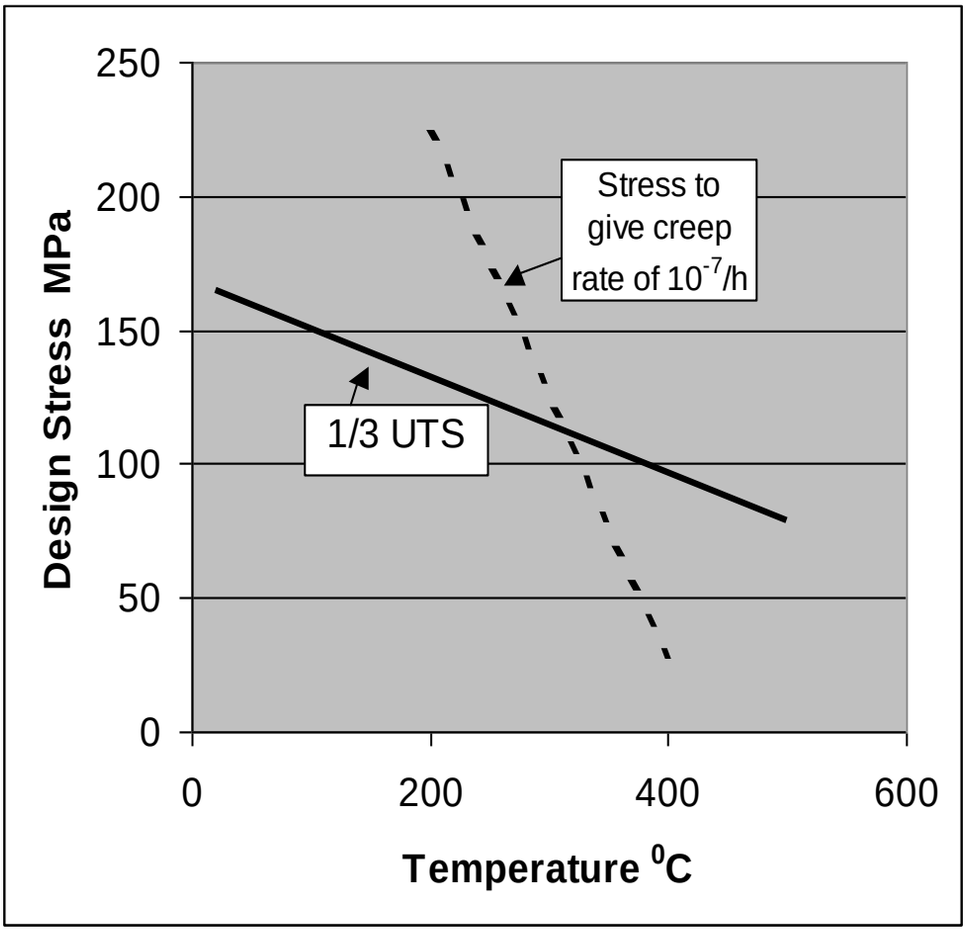

Figure 2-1: Schematic diagram showing temperature regions where the design stress of a hypothetical zirconium alloy is controlled by short-term and long-term mechanical strength.

Such a simple representation has been criticised because not only is it empirical but it does not necessarily fully capture the load-elongation curves. The exponential version is sometimes found to be superior to the power law representation [Balakrishnan & Chatterjee, 1993]. The power law approach is poor at describing variable loading history whereas an approach using differential constitutive relations can deal with changing conditions [Kocks, 1982]. Despite these reservations, in this section the parameters of Equation 2-1 are used to illustrate and compare the effect of test and metallurgical variables on work and strain-rate hardening because historically most reports of tensile properties do not include the full load-elongation curve that would be required to derive the power law, exponential function or the differential description. Equation 2-1 is used by the US NRC in their codes for calculating stress and plastic deformation in fuel cladding, especially for accident analysis [Siefken, 2001].

The values of constant h vary from zero, perfect plasticity, to 0.5, representing maximum dislocation generation [Kocks & Mecking, 2003]. The values of m vary from close to zero up to 1.0; they depend

on the thermally activated mechanisms represented by the activation volume, v^*, for a particular barrier to dislocation motion at temperature T [Conrad, 1965; Wei et al., 2004]:

Equation 2-2:

$$m \propto k_B T / v^* \sigma_T$$

where k_B is Boltzmann's constant

T is test temperature (K)

The shape of the load-elongation curve depends on specimen geometry and rates of work-hardening and strain-rate hardening. A tensile test on a bar of uniform cross-section at a constant cross-head rate will exhibit a maximum load because the loss of cross-sectional area and decrease in strain-rate cannot be completely compensated by work hardening. The true strain to maximum load, ε_{ml} is given by [Hart, 1967]:

Equation 2-3:

$$E_{ml} = h/(1+m)$$

Necks form in real specimens, which are allowed, by the standards, to have a central taper on cross-sectional area of up to 2%. The development of a neck also depends on small variations in microstructure and work-hardening and strain-rate hardening [Hart, 1967; Campbell, 1967; Coleman et al., 1976; Jonas et al., 1976; Ghosh, 1977; Kocks et al., 1979; Nichols, 1980]. Using a general stability criterion [Hart, 1967], the strain to the start of necking, ε_n, is given by:

Equation 2-4:

$$\varepsilon_n = h/(1-m)$$

The strain to maximum load is smaller than the strain to the onset of necking but when m is small the two strains will be similar. Note that attainment of a maximum load has nothing to do with the formation of a neck, although the elongation to maximum load is often called uniform strain; the strain to maximum load (in a perfect specimen) and the strain to the start of detectable necking (in a real specimen) simply almost coincide when values of m are low, and especially when the load-elongation curve is almost flat after yield.

Total elongation is the sum of uniform elongation and elongation during necking up to final rupture, which is initiated by internal cavity or pore formation. Total elongation depends on specimen length because, although elongation to maximum load is independent of specimen length for unirradiated materials, necking localises deformation and is a higher proportion of a short specimen than a long specimen; using total elongation as the measure of ductility, a short specimen will appear more ductile than a long specimen. To aid comparison between materials, in the standards the ratio of the gauge length to diameter is specified at four (or five in the metric version). For flat specimens the ratio of gauge length (ℓ), to specimen width (w) is set at four. In thin material the ratio of specimen width to thickness (t), can also affect measurements of ductility based on original length (ε_l), width (ε_w), or thickness (ε_t) [Ells & Cheadle, 1969]. For example, in tensile tests on Zircaloy-2 at room temperature with t = 1.5 mm, the strains to fracture varied with w/t, Figure 2-2. Here the strain to fracture is ln(final dimension/original dimension). At ℓ/w = 4, for this material w/t = 8.3 and ductility appears to become independent of w/t. In practise the shape and dimensions of the specimen should always be noted because circumstances, such as sampling components from power reactors [Adamson et al., 1986], may force the use of specimens that do not meet the standard.

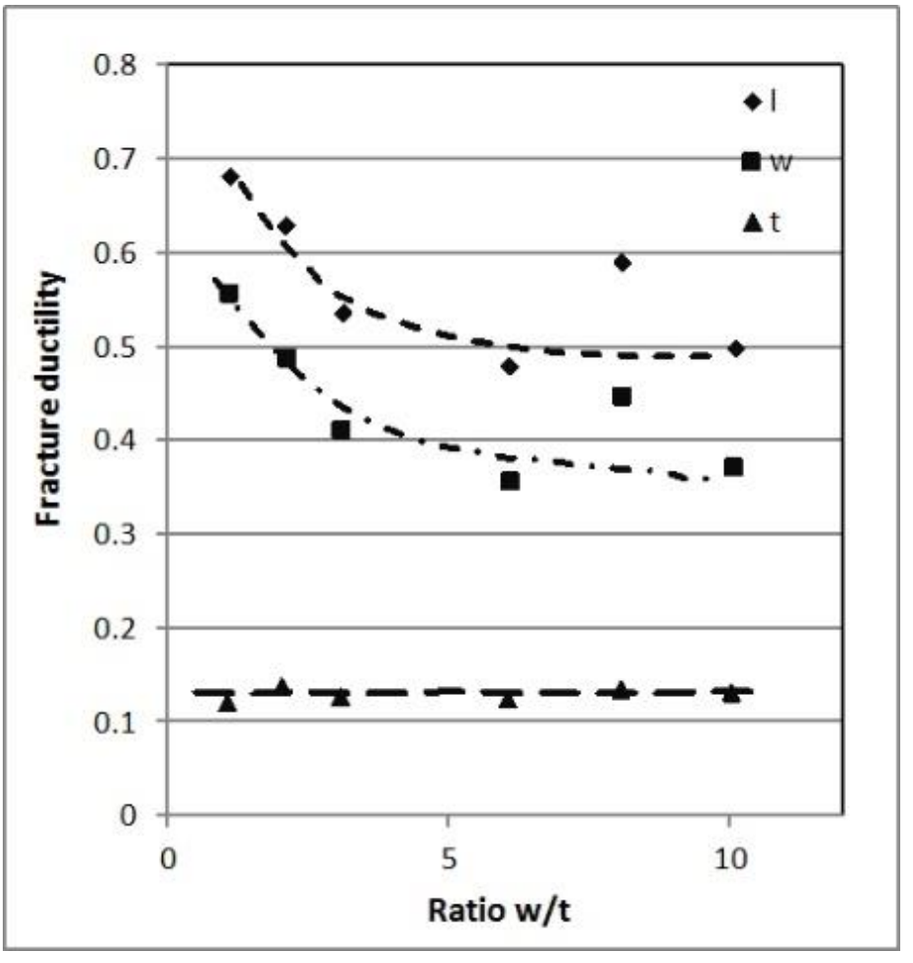

Figure 2-2: Fracture ductility of cold-worked Zircaloy-2, based on length, ε_ℓ, width, ε_w, or thickness, ε_t, at room temperature as a function of w/t. With t=1.5 mm, to meet ASTM Standard w/t should be 8.3 [Ells and Cheadle, 1969]

Necking is very sensitive to geometry and strain-rate hardening, a high value of m suppressing neck development. The value of m is determined as $d(\log \sigma)/d(\log \dot{\varepsilon})$. Defining $\sigma = P/A$, where P is the load imposed on a cross-section of area A and assuming no work-hardening, then because at any point along a specimen in tension $\dot{\varepsilon} = -1/A(dA/dt)$, it follows that $-(dA/dt) = (P/A)^{1/m}[A^{(m-1)/m}]$. With $m<<1$, smaller cross-sections reduce more rapidly than larger cross sections and necking follows. As m approaches 1.0, the shape of an incipient neck is preserved and large elongations are expected. Consequently, a large variation of ductility is possible depending on h and m. Figure 2-3 compares the data from many materials [Woodford, 1969] with the calculations of the effects of wide ranges of h and m on total elongation for a tensile specimen with a taper of 2% [Coleman et al., 1976].

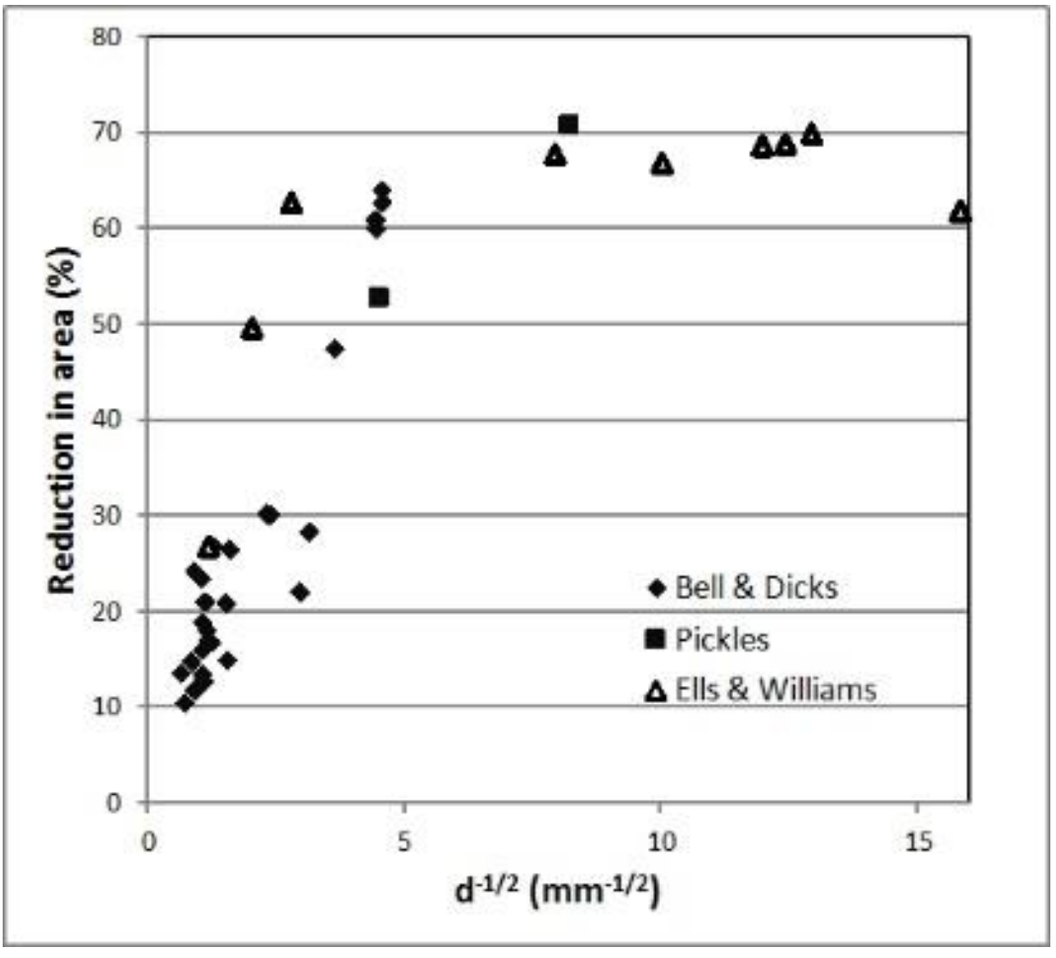

Figure 2-28: Dependence of reduction in area on β-grain size in quenched Zr-2.5 Nb. [Based on Bell & Dicks, 1965; Pickles, 1972; Ells & Williams, 1969].

2.1.3 Behaviour of irradiated material

The mechanisms and effects of irradiation on the mechanical properties of zirconium alloys are described Section 4. A wide response of these properties to irradiation has been reported that depends on the starting microstructure and the conditions of irradiation and testing. At reactor operating temperatures (250 to 360 °C (520 to 630 K)), the strength increases between 10 and 80% up to a fluence of about $3x10^{24}$ n/m^2 (E > 1 MeV); in general, the larger proportional increase is obtained with weak starting materials and vice versa. The transient is followed by a gradual increase in strength with neutron fluence, Figure 4-14 and Figure 4-15. As a further example, compared with unirradiated material, the proportional response of annealed Zircaloy to irradiation temperature is illustrated in Figure 2-29 for uniaxial tensile tests in the ranges 27 to 227 °C (300 to 500 K) and 250 to 410 °C (520 to 680 K) [Howe & Thomas, 1960; Bement, 1963; Bement, 1966; Hardy, 1970; Coleman et al., 1972; Rosenbaum et al., 1974; Cheadle et al., 1974; Holt, 1974b; Ells et al., 1974; Baroch, 1975; Onchi et al., 1977; Ells et al., 1985; Adamson & Bell, 1986; Morize et al., 1987; Yasuda et al., 1987; Wei et al., 2007; Cockeram et al., 2011]. The values represent a wide range of neutron flux and maximum fluence in each study and show that the increase in strength could be close to 300%. Despite the similarity of the starting materials, the data are very scattered, which is attributed to flux affects at high temperatures and fluences not always exceeding a threshold of about $3x10^{24}$ n/m^2. Test temperature only seems to affect the strength after irradiation in the range 250 - 360 °C (520 - 630 K), where much irradiation hardening can be attained. A maximum in the hardening with the higher test temperatures seems to be associated with this range in irradiation temperatures. This effect may be caused by a suppression of strain aging allowing full irradiation hardening. As the irradiation temperature is increased beyond 360 °C (630 K), the irradiation damage starts to anneal out as fast as

it is produced and the hardening diminishes. This high temperature response is strongly affected by neutron flux, with a high flux raising the temperature for no hardening.

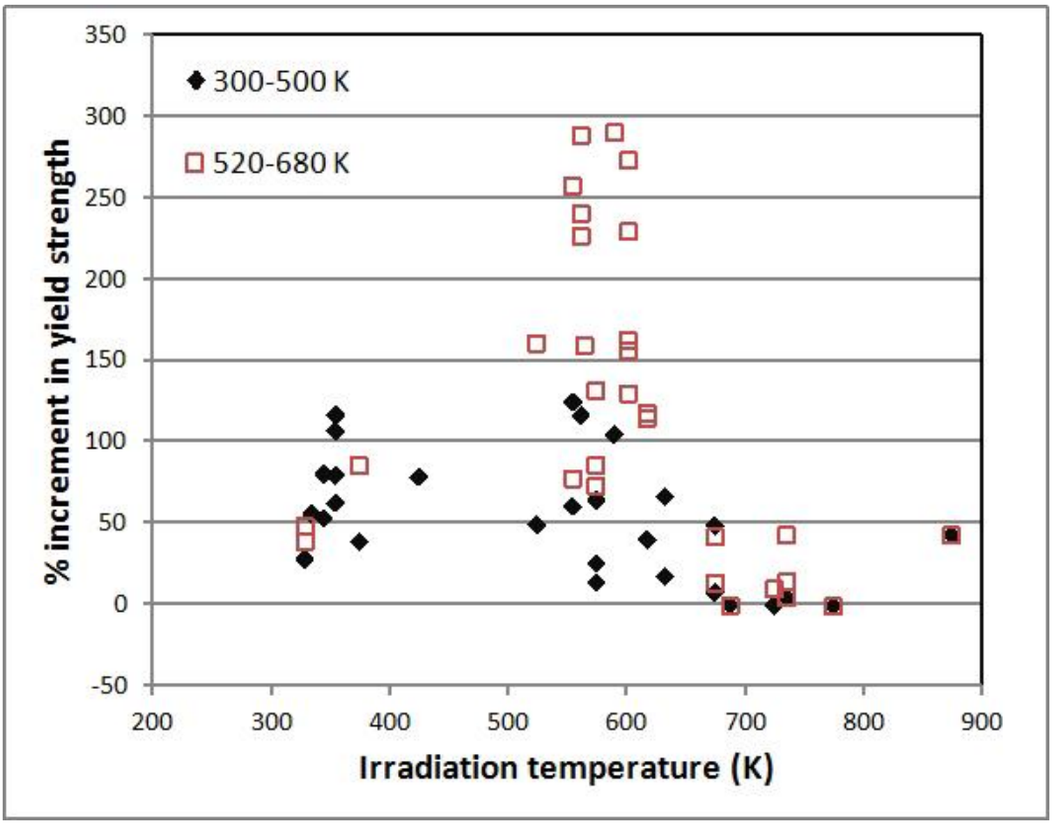

Figure 2-29: Effect of irradiation temperature on increment of yield strength of annealed Zircaloy tested in the ranges 300 to 500 K (27 to 227 °C) and 530 to 680 K (259 to 419 °C).

Dislocation loops developed during irradiation are responsible for the strengthening. During tensile testing, mobile dislocations can annihilate the loops in narrow bands (or channels or swaths), Figure 4-9 and Figure 4-10. Softening is observed associated with this loss of the strengthening agents, and the maximum load is attained at low strains, Figure 1-5 and Figure 1-6. This phenomenon is an example of the development of plastic instability in strengthened metals through strain softening [Luft, 1991]. With subsequent strain the regions cleared of irradiation damage start to develop dislocation cells indicating work hardening [Coleman et al., 1972]. When ductility is measured by total elongation, it is mostly affected through the loss in uniform strain. The mode of fracture is by cavity coalescence and the fracture surface consists of ductile dimples because, although the second phases may change, the underlying grain structure and composition (apart from a minor amount of transmutation) are not affected by irradiation. Reduction in area is not always impaired by irradiation to the same extent as elongation. Some examples follow.

The clearing out of irradiation damage depends on irradiation conditions, amount of strain, test temperature, and material texture, composition and microstructure. Irradiation damage locks the sources of mobile dislocations and a high stress is required to activate them – hence irradiation strengthening. Once activated, avalanches of dislocations sweep away the irradiation barriers and create a softened zone that ends at a grain boundary or is restricted by other microstructural features, such as dislocation cell structures in cold-worked material [Coleman et al., 1972; Himbeault et al., 1994]. The tendency to form channels increases as the yield strength of the material rises with amount of irradiation leading to a threshold fluence. For example, a threshold fluence for the formation of channels was indicated in annealed Zircaloy-2 irradiated between 150 and 200 °C (423 and 473 K); after deformation at 320 °C (593 K) material irradiated to 3.0×10^{24} n/m^2 contained channels whereas material irradiated to 3.2×10^{23} n/m^2 did not [Onchi et al., 1983]. Also, in annealed Zircaloy-4 irradiated at ≤ 100 °C (373 K) and tested at room temperature, channels were only observed in

material irradiated to a fluence ≥ 6.7 x 10^{22} n/m^2 (0.01 dpa); these channels were observed on prism planes [Farrell et al., 2004]. Channels free of irradiation damage are observed before their effect is manifest on a macro-scale as a load drop [Onchi et al., 1980; Fregones et al., 2000; Onimus, 2004]. Since less force is required to maintain further deformation after the initial channels are formed, new sources of dislocations are difficult to activate in the surrounding strong material in the original grain and the increase in the number of channels declines. The deformation is heterogeneous; in annealed alloys tested at 350 °C (623 K), between 40 and 60% of the grains contained narrow channels. The width of the channels, Figure 2-30, and their spacing seems to have a weak dependence on the irradiation fluence, but none on test temperature or plane of the channel.

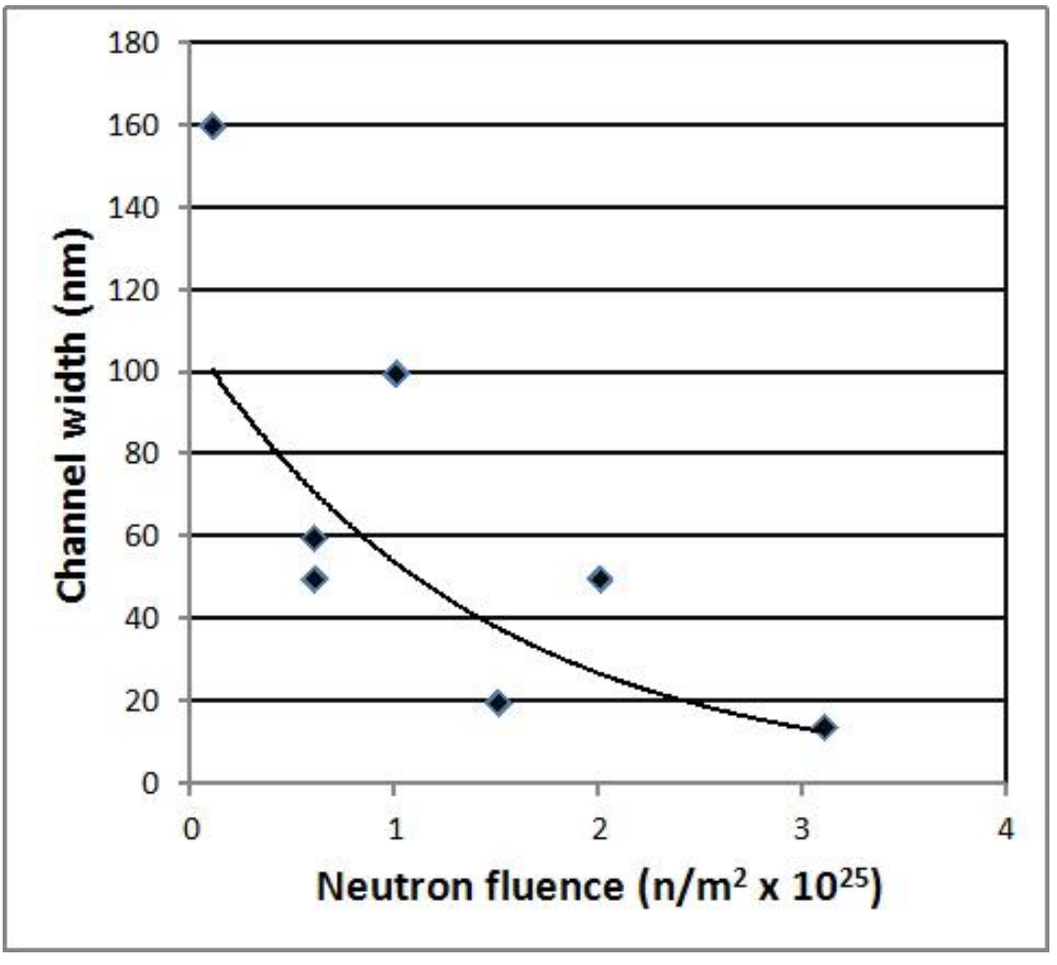

Figure 2-30: Decrease in width of channels cleared of irradiation damage as a function of neutron fluence.

The volume fraction of basal plane channels saturated by 0.5% plastic strain [Onimus et al., 2004]. The confined strain within the channels can be very high, over 100% [Williams et al., 1974] producing high stresses at the grain boundaries that may lead to new channels in the adjacent grains [Onchi et al., 1980; Onimus et al., 2004], and displacement at the boundaries [Lee & Adamson, 1977; Williams et al., 1974] or surfaces [Fregonese et al., 2000]. As the material is deformed, the original channels work-harden and dislocation cells form in material free of irradiation damage [Coleman et al., 1972; Fregonese et al., 2000; Regnard et al., 2002]. Subsequent deformation continues to be restricted and appears as shear bands that are visible to the naked eye on the surface [Bement, 1966; Coleman et al., 1972; Fregonese, 2000].

In the case of steels that are highly susceptible to irradiation embrittlement, the loss of toughness can reduce the safety margins so much that a decision has to be taken. Either the plant is shut down and decommissioned or a thermal recovery treatment is performed to anneal the irradiation damage. Such an annealing has been performed on early VVER 440 in Russia, having high Cu and Ni contents in the welds. Heat treatments of the RPV of 100-150 hours at 475 ± 15 °C allowed a recovery of the RT_{NDT} shift by more than 80 % and a significant operation life extension [Platonov, 2002]. The recovery was not as efficient for high Ni steels [Kryukov, 1998]. The difference in recovery efficiency could probably be explained by the difference in thermal stabilities of the CRC and MNSP. The atom probe examination of the clusters after irradiation and annealing heat treatments, showed that the recovery mechanisms are complex, with different kinetics of resolution for Cu and Ni. In addition, the behaviour of P, that catalyses the formation of clusters after two recoveries, could drastically change subsequent re-irradiation embrittlement [Kuleshova et al., 2018]. These complex phenomena have to be analysed in connection with the studies on the thermal stability of the different types of clusters [Almirall et al., 2019].

2.2.2 Austenitic stainless steels

2.2.2.1 Industrial alloy development

The need for corrosion resistant Fe based alloys received engineering solutions during the beginning of the 20th century when Fe alloys with significant additions of chromium were first processed. It was rapidly found that different types of stainless steels could be obtained, depending on the composition of the alloys. Basically, a minimal addition of Cr was required to be 13 % for room temperature corrosion resistance, while more than 18-20 % appeared to be necessary for good behaviour above 400 °C.

Such high Cr alloys exhibited a rather inconvenient ductile-brittle transition at low temperatures, a specific behaviour of the bcc ferrite. To avoid this undesirable behaviour, high Ni alloys were developed, to maintain these alloys in the high temperature fcc structure and not subject to this brittle behaviour at low temperature. The series of the 300 stainless steels have been developed from these early observations and were continuously improved.

The relative amount of Cr and Ni drives the microstructure of the alloys after quenching from high temperature, as seen in Figure 2-52. The high cost of Ni leads to minimising the Ni content required to have an fcc structure at room temperature: the two main alloys are just at the lower limit of the austenite phase (fcc). Therefore, the austenite of these alloys may be slightly unstable and can return partly to a bcc structure, either thermodynamically or by strain-induced transformation. The Ni free, ferritic stainless steels (400 series) are not of concern for nuclear applications, and will not be described further.

The alloys currently used in nuclear cores elements, are limited to the 304 and 316 alloys. Their compositions are given in Table 2-5.

- 304 SS is the basis of the austenitic steels. For the high temperature corrosion resistance, it required a Cr concentration of 18%. The Schaeffler diagram (Figure 2-52) shows that with this Cr concentration, a minimal Ni content of 8-9 % is required to maintain the fcc structure after solutions anneal at high temperature.

- 316 SS is a variant of the 304 alloys, with an addition of Mo, at a concentration of 2-3%.

In these austenitic steels, manganese at a concentration of 1-2 %, and silicon at 0.5-1%, are present for processing reasons, without significant effect on properties.

Table 2-5: Composition of various commercial austenitic stainless steels (wt%).

Alloy	Cr	Ni	Mo	Mn	Si	C	Ti	Nb	Others
304	18-20	8-12	-	1-2	0.75	0.08	-	-	304L (0.03C), 304LN
316	16-18	10-14	2-3	2	0.75	0.08	-	-	(0.03C, <0.14N)
321	17-19	9-13	-	1-2	0.75	0.04-0.08	0.2-0.4	-	316L (0.03C), 316LN
347	17-19	9-13	-	1-2	0.75	0.04-0.08		0.4-0.8	(0.03C, <0.14N)

At high temperatures, above 1000 °C, the alloying elements are all in solid solution, forming an austenite of fcc structure. This structure is not stable at lower temperatures: Cr tends to interact with C to form carbides. If a quench is performed from the 1000-1050 °C range (solution anneal) the solid solution is maintained in a metastable state. Any intermediate heat-treatment, such as the heat-affected zones of welds, allows the alloy to transform to its equilibrium state, and chromium carbides precipitate. During this precipitation process, the carbon, a fast diffuser, migrates from the bulk of the grains to the grain boundaries (GB), where it interacts with the chromium. But the slow diffusing chromium only migrates from the vicinity of the GB. The result is a local depletion in Cr of the matrix near the GB. This depletion can be so high that locally the corrosion resistance may be lost, leading to an intergranular corrosion in the heat-affected zones of the welds of 304 or 316 alloys.

To inhibit this chromium depletion due to carbide precipitation, two solutions have been developed:

- Lowering the carbon concentration (L series) 304L and 316L, that is efficient, but requires a more complex processing;
- Avoid the formation of chromium carbides, with additions of chemical elements of high affinity for carbon. The corresponding alloys are 321with Ti additions, and 347, with Nb.

Nitrogen was found to have a significant effect when in solid solution by increasing the yield strength. The corresponding alloys (304LN…) are mostly used in non-nuclear industry and will not be detailed. A surface treatment such as the ion-nitriding process improves the wear resistance of mobile elements in the core. If performed on 321, it would lead to an interaction of nitrogen with titanium in the heat-affected zone, forming TiN precipitates. These precipitates have higher formation free energy than TiC. The consequence of TiN formation is that Ti is no longer available to trap C as TiC and Cr can then interact with C to form chromium carbides. Then the stabilizing effect of Ti (or Nb) described above no longer exists.

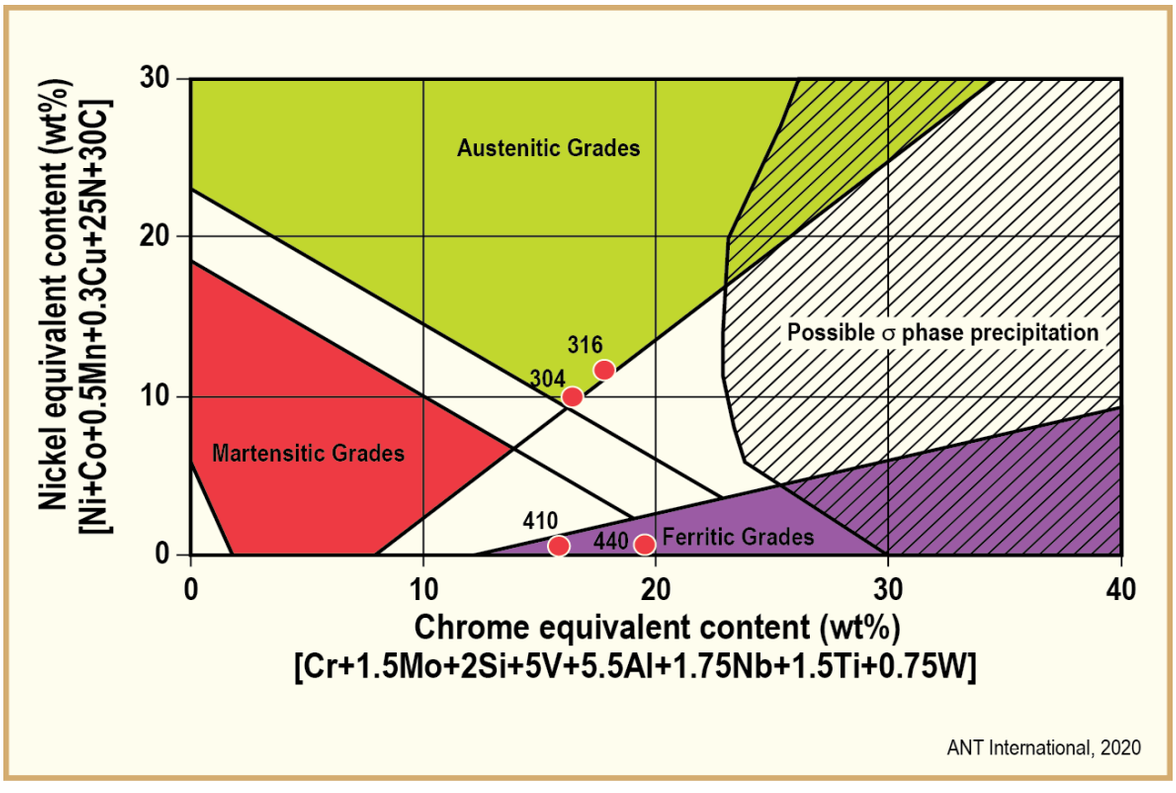

Figure 2-52: The Schaeffler diagram for Cr-Ni stainless steel structure predictions. [After https://www.langleyalloys.com/es/a-guide-to-duplex-super-duplex-and-hyper-duplex-stainless-steels/].

Phases and structure

At high temperatures, above 1050 °C, all these steels are homogeneous, in solid solutions with fcc structure. Since there are no second phases, nothing restricts the grain growth during any solution anneal heat-treatment. The resulting structure consists of recrystallized, equiaxed grains of rather large size, typically 50 - 100 µm. Unless heavily cold rolled, no crystallographic texture is produced, and the physical and mechanical properties are quasi-isotropic. Often a limited cold-work is performed after the solution anneal (straightening 1-3%), that increase slightly the yield strength. For thin foils, the recrystallization treatment after cold-rolling allows a reduction of grain size down to 1-10 µm.

At high temperatures corresponding to the solution annealing treatment (980 -1050 °C) the alloys are homogenised as a solid solution. This γ–phase is not fully stable at room temperature. Various intermetallic phases are known to precipitate at intermediate temperatures. These phases have been reviewed by Lo et al. [Lo et al., 2009]. Most of them do not appear at temperatures of interest in thermal nuclear power reactors. The precipitation temperatures are in the range of 650 - 950 °C for most of the phases [Maziasz, 1987].

The only matter of concern is the precipitation of chromium carbide, earlier described and the formation of the σ–phase in the case of locally Cr enriched alloys [Hsieh, 2012]. The effect of the σ–phase is its brittle behaviour, due to its crystallography. The σ–phase in binary Fe-Cr alloys is a simple compound of formula FeCr, with a tetragonal crystal structure. In the case of multicomponent alloys, a generic formula of the σ–phase corresponds to $(Fe,Ni)_x(Cr,Mo)_y$. This phase precipitates at high temperatures and can therefore be found in the case of thick welds where the cooling rate is low, allowing the alloy to remain durable at temperatures high enough for this phase to precipitate. For thin components, the phase is not expected to occur in reactor operations. These phases form only during the fabrication steps, and are not expected to appear during operation.

The fcc austenite has a Young's modulus around 200 GPa, and a thermal expansion coefficient near $17x10^{-6}$ K^{-1}, i.e. 50% higher than that of the bcc steels. This difference between bcc and fcc steel in thermal expansion coefficients has to be considered for strain compatibility when such different alloys

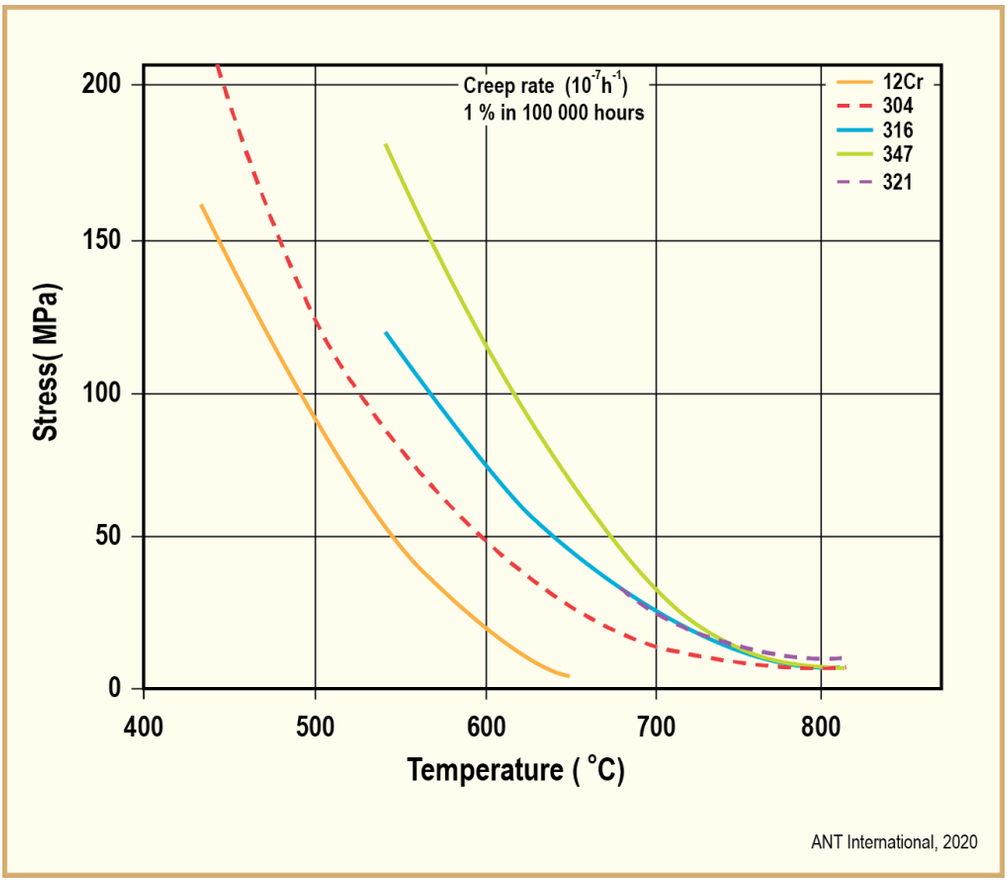

Figure 2-57: Creep-Rate Curves for Several Annealed Stainless Steels [American Iron & Steel Institute, 2002].

2.3 Mechanical Properties of Nickel-Based Alloys

Nickel alloys are used extensively throughout the nuclear industry because of their durability and resistance to corrosion and mechanical property degradation at high temperatures. When nuclear plants were first constructed, the performance of Ni-alloys over the long periods of nuclear reactor operation in the reactor core were not fully known. Over the past 60-70 years improved Ni-alloys have been developed to suit the particular operating conditions in nuclear reactor cores [Boothby, 2012; Yonezawa, 2012; Strasser and Ford, 2012]. For Ni-alloy components used in fuel assemblies and other power reactor core internals, improvements have been directed mainly at mitigating stress corrosion cracking, particularly for the weld metals and transition pieces used to make the joints between the external pressurised piping and the openings in the pressure vessel that allow for the insertion of control rods and other device insertions. Stress corrosion cracking is also responsible for failures of fasteners (bolts) in core internal structures and hold-down springs in some of the early fuel assembly designs [Strasser and Ford, 2012]. Stress corrosion cracking is a high stress phenomenon that is exacerbated by irradiation [Andresen and Was, 2012], i.e. irradiation assisted stress corrosion cracking (IASCC).

The properties of Ni-alloys used in power reactors have been reviewed by Yonezawa [Yonezawa, 2012]. The applications and behaviour of Ni-alloys used in power reactor cores has been reviewed by Strasser and Ford [Strasser and Ford, 2012], Griffiths [Griffiths, 2014; Griffiths, 2019] and Stopher [Stopher, 2017]. The review by Griffiths [Griffiths, 2019] addressed the use of Ni-alloys in all reactor types as well as ion irradiation facilities. Ni-alloy usage in Generation-IV and fusion applications have been addressed in the reviews by Rowcliffe et al. [Rowcliffe et al., 2009] and Maloy et al. [Maloy et al., 2013]. Applications for extra-terrestrial reactors has been reviewed by Angeliu et al. [Angeliu et al., 2007].

2.3.1 Development of Ni-alloys for use in Nuclear Reactors

Research into the effects of irradiation on nickel-based alloys peaked during the fast reactor development programs carried out in the 1970s and 1980s. Interest in these materials focused on their resistance to irradiation-induced void swelling compared with austenitic steels, although a perceived susceptibility to irradiation embrittlement limited their application to some extent. Nevertheless, the Nimonic alloy PE16 was successfully used for fuel element cladding and sub-assembly wrappers in the United Kingdom, and Inconel 706 was used for fuel cladding material for fast reactors in France. Both of these materials are precipitation-hardened and consequently have high creep strength, and much research and development on alternative alloys was directed toward maintaining swelling resistance and creep strength while aiming to alleviate, or at least understand, irradiation embrittlement effects. The properties of Ni-alloys pertinent to fast reactor operation were discussed in the review by Boothby [Boothby, 2012]. Precipitation-hardened Ni-alloys are also used extensively in conventional thermal power reactors, primarily as springs and spacer grids in fuel assemblies and fasteners (bolts) in the internal structures. The main spring materials used in fuel assemblies in thermal reactors are Inconel X-750 and Inconel 718 in the precipitation-hardened condition.

Nickel alloys are used extensively in nuclear reactor applications because they have high strength and good corrosion properties. Nickel has some nuclear properties (including relatively high thermal neutron absorption cross-sections) that limit its use in power reactor cores to specialized components, such as springs and high strength fasteners, that are subject to low neutron doses over their service life. Ni-alloys are particularly prone to He embrittlement, not only because of the presence of B that can produce He at low thermal neutron fluences, but also because of the transmutation of the main natural isotope, ^{58}Ni, to ^{59}Ni, which has a high thermal neutron capture cross-section, resulting in damaging H and He production at high thermal neutron fluences. The two-stage process, involving transmutation of ^{58}Ni to ^{59}Ni, constitutes a mechanism for irradiation-induced degradation due to He embrittlement that is unique to Ni amongst common engineering alloys. In fast reactors, Ni is also prone to He generation from the high energy (n,α) reaction, which has a cross-section that is an order of magnitude higher compared with the other main alloying elements, Fe and Cr [Mahmood et al., 2018].

Table 2-6 adapted from the various reviews [Boothby, 2012; Yonezawa, 2012; Strasser and Ford, 2012], lists the nominal compositions of the common Ni-alloys that are currently in use, or have been used, in nuclear reactors. A review of corrosion, stress corrosion cracking and irradiation-assisted-stress-corrosion-cracking of Ni-alloys in reactor systems has been given by Andresen and Was [Andresen and Was, 2012] and by Fyfitch [Fyfitch, 2012]. The review by Fyfitch also provides a detailed description of where Ni-alloys are used in existing nuclear power plants. Table 2-7 lists the minor elements and impurities that can have a significant effect on the Ni-alloy properties.

Ni-alloys are distinguished from austenitic, martensitic and ferritic steels, which also contain Ni, by the amount of Ni. Alloys containing less than about 28 wt% Ni are generally considered to be steels. The alloys listed in Table 2-6 are all FCC-based (the γ-phase) because of the high Ni concentration. Apart from Fe and Cr, there are a number of elements that are soluble in Ni (e.g. Al, Ti, Nb, Mo) thus providing a large range of possibilities for solid-solution-strengthening and also precipitation-hardening. Most of the alloys listed in Table 2-6 are precipitation-hardenable, primarily from the creation of ordered Υ' or Υ'' phases, although many alloys also contain grain boundary carbides that are desirable for high temperature creep resistance. The Υ' is an ordered FCC phase based on Ni_3Al and the Υ'' is an ordered BCT phase that is based on Ni_3Nb, with the possibility of substitution of small amounts of Fe/Cr in place of Ni and Ti/Ta/Nb or Ti/Ta/Al in place of Al or Nb respectively [Strasser and Ford, 2012]. Alloys that are not hardenable by Υ' or Υ'' precipitate formation include Alloy 600, 800 and Hastelloy X.

Table 2-6: Nominal compositions (wt%) of commercial Ni-based alloys.

Alloy	Ni	Cr	Fe	Ti	Al	Nb	Mo	Co	W
Nimonic PE16	43	17	33	1.2	1.3		3.7		
Inconel 750	72	15.5	7	2.5	0.7	1			
Inconel 718	53	18	19	0.9	0.6	5	2.5		
Inconel 706	42	16	37	1.7	0.3	2.9	0.1		
Inconel 690	61	29	9	0.5	0.5				
Inconel 625	61	22	5*	0.3	0.3	3.5	9		
Inconel 600	75	16	8	0.3	0.2				
Incoloy 800	33	21	39.5^	0.4	0.4				
Hastelloy X	47	22	18	0.15*	0.5*		9	1.5	0.6
Hastelloy N	71	7	4*	0.15*	0.5*		16		0.5*

* Max, ^ Min

Table 2-7: Maximum allowed minor alloying/impurity elements (wt%) of commercial and developmental Ni-based Alloys.

Alloy	Mn max	Si max	C max	Cu max	P max	S max	B max	Co max
Nimonic PE16	0.1	0.2	0.05					0.05
Inconel 750	1.0	0.5	0.08	0.5	0.008	0.01		0.05
Inconel 718	0.2	0.2	0.04	0.3	0.015	0.015	0.006	0.05
Inconel 706	0.2	0.2	0.03			0.015		0.05
Inconel 690	0.5	0.5	0.05	0.5	0.025	0.015		0.05
Inconel 625	0.2	0.2	0.05	0.3	0.015	0.015	0.02	0.05
Inconel 600	0.2	0.2	0.08	0.3	0.1	0.015		0.05
Incoloy 800	0.9	0.5	0.08	0.5	0.03	0.03		0.05
Hastelloy X	1.0	1.0	0.15	0.5	0.04	0.03	0.01	-
Hastelloy N	0.8	1.0	0.06	0.35				0.02

The response to irradiation depends very much on the microstructure of the various alloys. The behaviours of precipitation-hardenable nickel-based alloys such as Inconel X-750 and Inconel 718 are sensitive to the heat-treatment that will result in either a solution annealed (SA) or precipitation hardened (PH) material, although in most cases precipitation-hardenable material is used in the hardened condition. The response to neutron irradiation is very sensitive to the Ni-concentration because of the unusual transmutation effect exhibited by Ni in which the commonest isotope ^{58}Ni (68% abundance) transmutes to ^{59}Ni by the capture of a thermal neutron. ^{59}Ni, in turn, has high neutron capture cross-sections for the (n,γ), (n,p) and (n,α) reactions for a large range of neutron energies extending into the thermal energy range. Ni-alloys are particularly prone to the effects of high rates of He generation in a thermal neutron environment after neutron exposure sufficient to generate appreciable amounts of ^{59}Ni. For this reason, this report will also include a section on nuclear

reactions in Ni before addressing the effect of irradiation: microstructural stability, void (cavity) swelling, irradiation embrittlement and irradiation creep that controls irradiation stress relaxation.

2.3.2 Physical Metallurgy

Nickel (Ni) has a face-centred-cubic (FCC) crystal structure and melts at 1455 °C. It is an element that forms the base for a group of alloys (that also includes those based on iron and cobalt) known as super-alloys; these are high-temperature materials that are resistant to mechanical and chemical degradation at temperatures close to their melting points [Beardmore et al., 1969]. The alloys listed in Table 2-6 are all FCC-based (the γ-phase) because of the high Ni content. The ternary phase diagram showing the approximate compositions of the three main alloying elements (Ni, Cr and Fe) for the alloys in Table 2-6 is shown in Figure 2-58, [Griffiths, 2019]. Hastelloy-N is omitted from this ternary plot because of the low Fe content for that alloy. The compositions in Figure 2-58 are approximate and have been normalised so that Fe + Cr + Ni = 100%. Apart from Fe and Cr there are a number of elements that are soluble in Ni (e.g. Al, Ti, Nb, Mo) thus providing a large range of possibilities for solid-solution-strengthening and also precipitation-hardening.

Some Ni-based super-alloys, containing precipitates of the ordered γ' phase with sufficient size and density, exhibit an unusual property in that the yield stress (YS) and creep resistance either increase or remain relatively constant with increasing temperature up to about 800 °C [Beardmore et al., 1969]. The γ' phase imparts a strengthening effect in the alloy that is a function of the γ' volume fraction, Figure 2-59. The γ' phase itself increases in yield strength with increasing temperature up to about 800 °C, whereas the γ phase exhibits a temperature dependence that is typical of most metals, i.e. metals tend to be softer (decreasing yield stress) with increasing temperature.

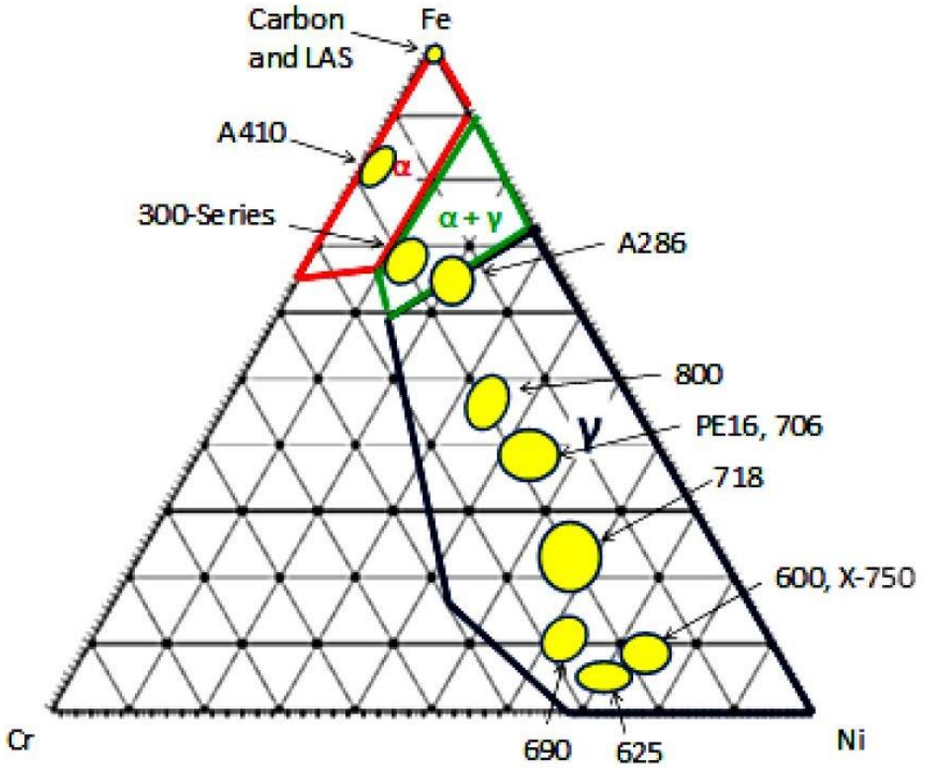

Figure 2-58: Ternary diagram for the Fe-Cr-Ni system at 400 °C illustrating the relative approximate compositions (considering Fe+Cr+Ni = 100 at%) of the main Ni-rich structural alloys in and their thermodynamically stable FCC phase (γ) compositions outlined in blue. The austenite phase in the green region is meta-stable leading to a wide range of austenitic, ferritic, martensitic and duplex stainless steels. The ferritic BCC phase (α) in the red region contains the high strength carbon and Low Alloy Steels (LAS) stainless steels used for pressure vessels and piping.

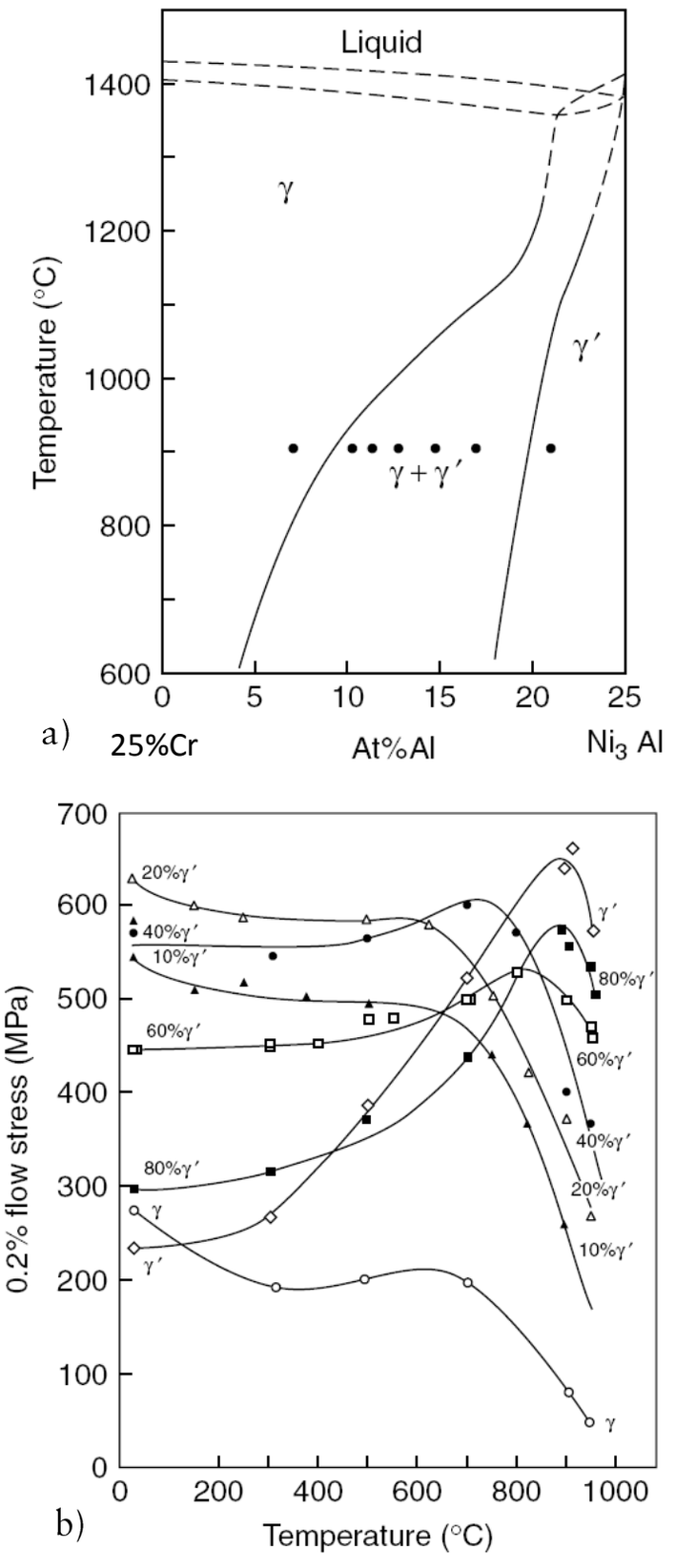

Figure 2-59: Temperature dependence of the yield stress for a number of Ni-Cr-Al alloys with 75 at%Ni and varying amounts of Cr and Al giving varying amounts of γ': (a) alloy compositions in the section of the ternary phase diagram at 75 at% Ni; (b) 0.2% yield stress as a function of volume fraction of γ' phase. Adapted, with permission, from Beardmore et al. [Beardmore et al., 1969].

The γ' phase has a composition of Ni_3X; it has an ordered FCC structure with the Ni atoms occupying the cube face positions and element X occupying the cube corners (Figure 2-60). For most of the γ'-containing Ni-alloys used in nuclear applications X is typically Al, but other elements (such as Ti, Nb and Mo) can also partially substitute for Al. The γ' phase is often coherent with the base Ni matrix and the compositional difference leads to a small misfit strain (typically <0.5% [Read, 2006]) thus producing strain contrast when imaged in an electron microscope.

With Nb present, a related ordered phase, γ'', which has a body-centred-tetragonal (BCT) structure and composition of Ni_3Nb, can be produced in addition to γ'. Carbon, present at concentrations up to 0.1 wt%, combines with reactive elements such as Cr to form carbides. Carbides often nucleate on grain boundaries during high temperature processing. They are favoured for very high temperature engineering applications in turbine blades because they restrict grain growth and grain boundary sliding during very high temperature operation [Read, 2006]. Carbides can also be detrimental to stress corrosion cracking (SCC) and there is no clear need for them in Ni-alloys used at the relatively low temperatures of nuclear applications [Strasser and Ford, 2012]. Boron acts in a similar manner to carbon and forms borides on grain boundaries if present in sufficient concentrations. Boron is a beneficial trace element for non-nuclear applications but has an adverse effect on high temperature stress corrosion cracking (HTSCC), and low temperature crack propagation (LTCP), of irradiated material for boron contents >20 wtppm [Mills et al., 1993]. Mills et al. [Mills et al., 1993] attributed the effect of the boron, in lowering fracture toughness and increasing SCC rates in irradiated specimens, to transmutation effects, either through the production of He or the production of Li. Boron is normally a trace element (<0.01 wt%, i.e. 100 wt. ppm) for alloys used in nuclear reactor cores. ^{10}B, which constitutes about 20% of the boron isotopes, has a very high thermal neutron (n,α) cross-section producing He. The maximum He concentration that can be produced is limited by the concentration of ^{10}B and is typically <100 appm for most engineering alloys.

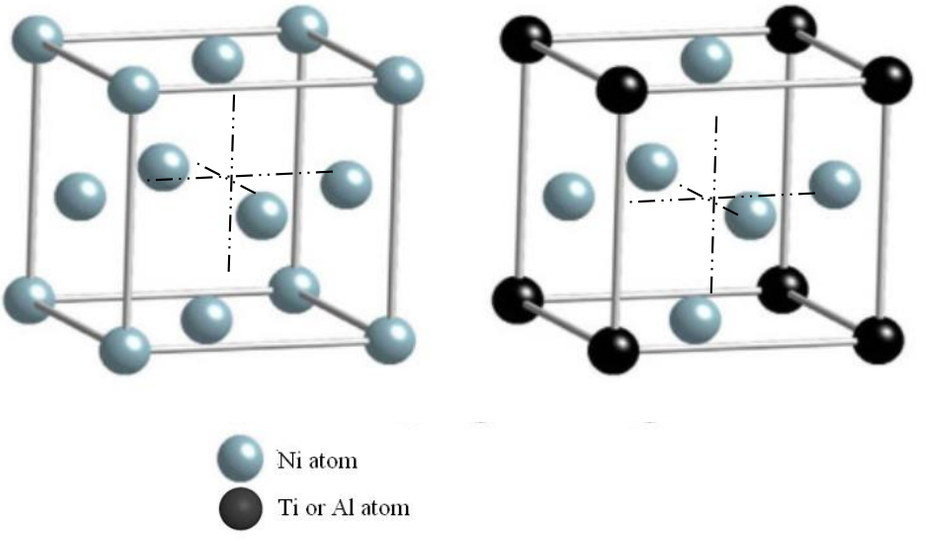

Figure 2-60: Crystal structure of FCC γ-phase (Ni) and γ'-phase ($Ni_3(Ti,Al)$).

The main elements that are important to the constitution of Ni-based super-alloys are shown in Figure 2-61 [Read, 2006]. The relative atomic sizes and electron vacancy numbers (N_v), i.e. the average numbers of electron vacancies per atom, give an indication of the likelihood that the alloying elements are either in solid solution (similar atomic size) or form the γ'-phase (large mean N_v), [Sims et al., 1987] . The common precipitate phases are listed in Table 2-8 [Strasser and Ford, 2012].

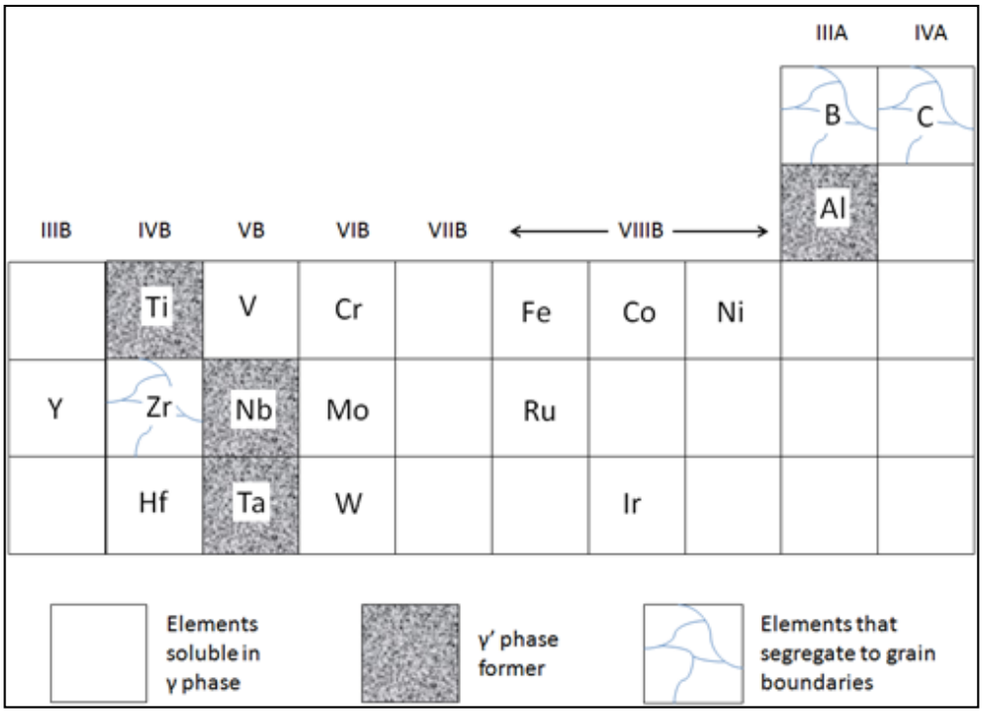

Figure 2-61: Summary of elements important to the constitution of the Ni-based super-alloys, and their relative positions in the periodic table.

Table 2-8: Phases in high strength nickel alloys. Adapted from Strasser and Ford [Strasser and Ford, 2012].

γ (gamma)	Face-Centred-Cubic (FCC)	Ni-Cr-Fe solid solution	Same structure as matrix for alloys 625, 718 and X-750.
γ' (gamma prime)	Ordered FCC	$Ni(Cr,Fe)_3Al(Ti,Nb,Ta)$*	Precipitation hardening phase for Alloys 718 and X-750, associated with coherency between the γ matrix and the precipitate. The γ' shape changes with aging time and temperature, varying between spherical and cubic.
γ" (gamma double prime)	Body-Centred-Tetragonal (BCT)	$Ni(Cr,Fe)_3Nb(Ti,Al,Ta)$*	Additional precipitation hardening phase for Alloy 718 with a disc-shaped morphology 60 nm diameter and 5-9 nm thickness.
δ (delta)	Orthorhombic	Ni_3Nb	Observed in over-aged alloy 718 as a transformation from the coherent γ"- phase. Morphology is acicular and since it is incoherent with the γ- phase there is minimal strengthening. Inter-granular formation acts as an inhibitor to grain growth
η (eta)	Hexagonal-Close-Packed (HCP)	Ni_3Ti	Observed in overaged alloy X-750 as a transformation from the coherent γ' phase. Morphology is acicular and since it is incoherent with the γ phase there is minimal strengthening. Inter-granular formation acts as an inhibitor to grain growth.
σ (sigma)	Tetragonal	FeCr, FeCrMo	Irregular shaped globules and plate morphologies formed after extended times at high temperatures (540-980 °C)

Table 2-8: Phases in high strength nickel alloys. Adapted from Strasser and Ford [Strasser and Ford, 2012], cont'd.

μ (mu)	Rhombohedral	$(Fe,Co)_7(Mo,W)_6$*	Coarse irregular Widmanstätten platelets formed at high temperatures in alloys with high Mo or W contents.
Laves	Hexagonal	Fe_2Nb, Fe_2Ti, Fe_2Mo	Irregular elongated globules or platelets after extended high temperature exposure.
MC	Cubic	TiC, NbC, HfC	Primary carbide formed during casting in inter-dendritic regions
M_6C	FCC	Fe_3Mo_3C	Primary carbide formed during casting in inter-dendritic regions.
M_7C_3	Hexagonal	Cr_7C_3	Inter-granular secondary carbides formed at intermediate temperatures with an accompanying Cr denuded zone.
$M_{23}C_6$	FCC	$(Cr,Fe,W,Mo)_{23}C_6$*	Inter-granular secondary carbides formed at intermediate temperatures, with an accompanying Cr denuded zone.
M_3B_2	Tetragonal	Ta_3B_2, Nb_3B_2	Borides observed in alloys containing > 0.03 wt.%B.
MN	Cubic	TiN, ZrN	Nitrides observed in cast structures with square to rectangular shapes.
* - brackets denote optional substitution			

The γ' and γ" phases are meta-stable and transform to the hexagonal close packed η (Ni_3Ti) and orthorhombic δ (Ni_3Nb) phases, respectively, with sufficient aging time. These η and δ phases do not contribute to precipitation-hardening because of their size, number density and lack of coherency with the γ matrix. They can be beneficial to mechanical properties when segregated to grain boundaries in restricted amounts since they can inhibit excessive grain growth in the same way as carbides. However, they can also be deleterious to mechanical properties due to their brittle nature and acicular morphology.

2.3.3 Thermo-Mechanical Processing

There are five generic types of heat treatment that have been developed for Ni-rich engineering alloys and each have a role in defining the temperature/time combinations required for specific phase formations [Strasser and Ford, 2012]:

1. *"Homogenization"* that is sometimes used, but rarely specified, at temperatures approaching the melting temperature. The objective is to diffuse out the gross solidification micro-chemical gradients, and to take into solution high melting point phases, such as primary carbides.

2. *"Solution Anneal"* (SA) applied in the range 890 °C - 1100 °C to take into solid solution those phases that impact on strength and structural integrity while precipitating some carbides on grain boundaries.

3. *"Direct Age"* (DA) refers to hot working followed immediately by aging at temperatures around 704 °C to precipitate out the hardening γ' and γ'' phases.

4. *"Single Step Aging"* refers to a single aging treatment around 704 °C following the solution anneal.

5. *"Double Step Aging"*, or *"Double Aging"*, refers to a double-step aging treatment following the solution anneal, with the first aging treatment at about 885 °C, followed by the second aging treatment around 704 °C to precipitate out the hardening γ' and γ" phases. The first age improves the stress rupture properties of alloys such as X-750 and 718 at temperatures >650 °C by promoting grain boundary precipitation (primarily carbides) that limits grain boundary sliding at high temperatures.

Each alloy has its own characteristic phase stability and transformation kinetics, see for example Figure 2-62 and Figure 2-63 [Smith and Patel, 2005]. These characteristics are of importance in specifying the thermo-mechanical treatments and the cooling rates. The size, shape and spacing of the γ' and γ" precipitates, determined by the heat treatment [Cozar and Pineau, 1973], are important in controlling the high temperature creep and yield strength. The various thermo-mechanical treatments are designed to produce specific metallurgical properties for different Ni-alloy components depending on their applications and are described in the appropriate manufacturers' alloy specifications [Special Metals Corporation, 2019].

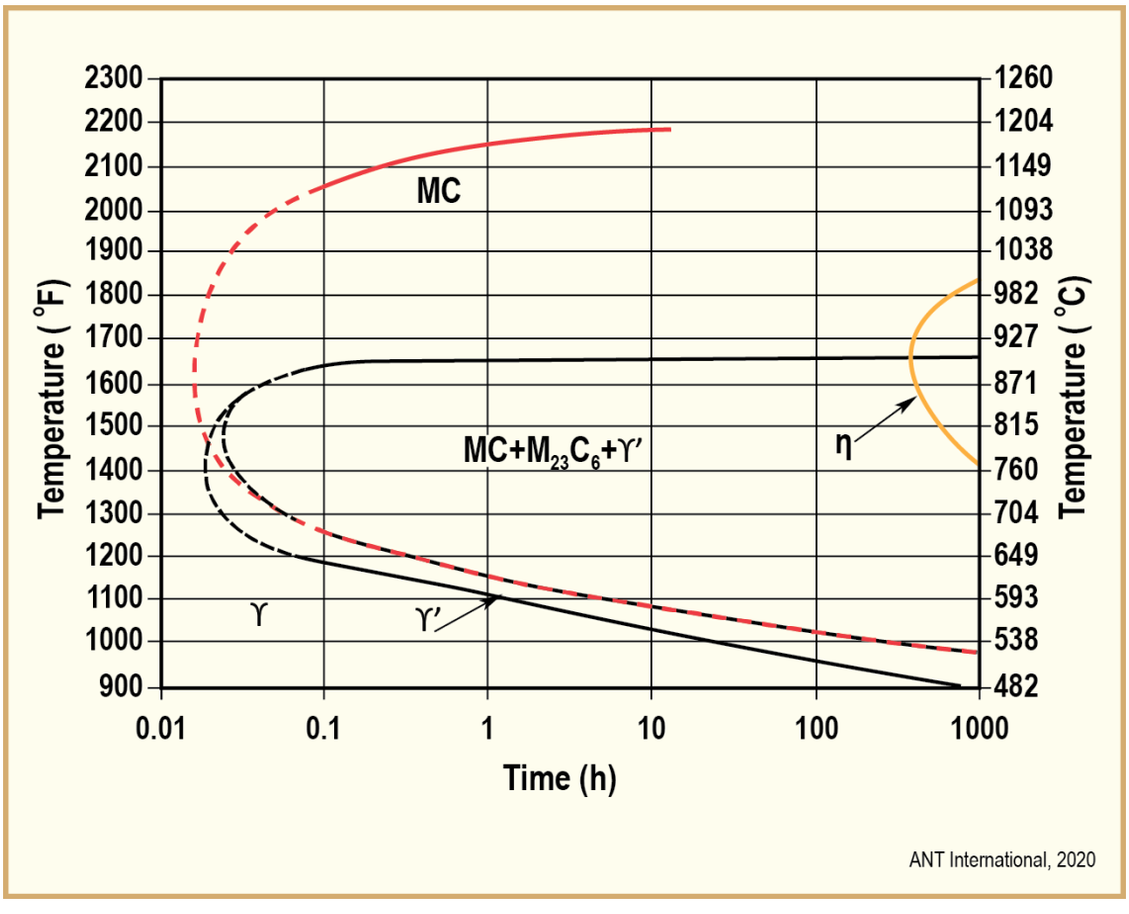

Figure 2-62: Time-Temperature-Transformation diagram for Inconel X-750 showing regions of carbide γ' and η precipitation, after Smith and Patel [Smith and Patel, 2005].

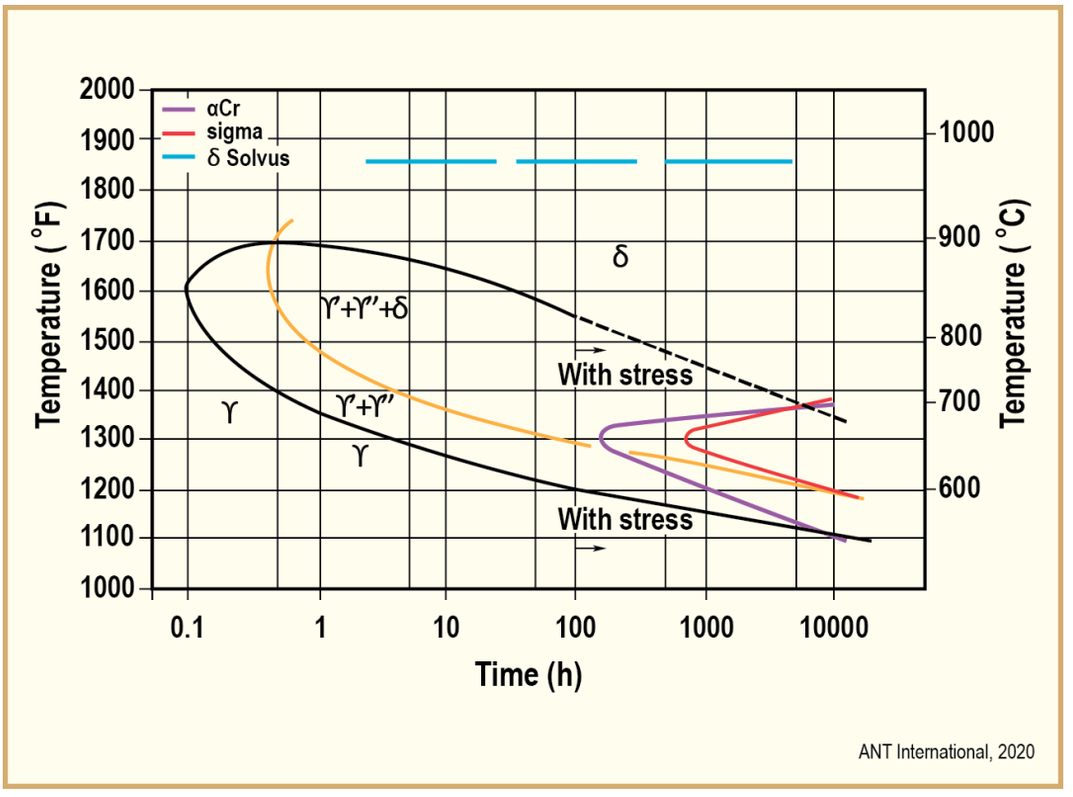

Figure 2-63: Temperature-time-transformation diagram for Inconel 718 showing variation of nucleation times for γ' and γ" phases, after Smith and Patel [Smith and Patel, 2005].

2.3.4 Mechanical Properties

There have been a number of reviews describing the mechanical properties and characteristics of Ni-alloys relevant to nuclear reactor applications, the most recent being that of Yonezawa [Yonezawa, 2012] for unirradiated alloys, and Boothby [Boothby, 2012], Rowcliffe et al. [Rowcliffe et al., 2009], and Angeliu [Angeliu et al., 2007] for irradiated alloys. One critical issue, pertinent to Ni-alloys in particular, is the propensity for He production in a thermal neutron environment [Greenwood, 1983].

The needs of the nuclear industry differ from those of the aerospace industry primarily because of the operation in a water, He, molten salt or liquid metal coolant environment, but both industries share common requirements for high strength and corrosion resistance. For the aerospace industry high temperature strength and creep resistance are important properties for Ni-alloys. Operation in an aqueous or moist environment is a requirement for most nuclear applications and therefore resistance to corrosion, SCC and irradiation assisted SCC (IASCC) is also important [Andresen and Was, 2012; Maloy et al., 2013; Fyfitch, 2012].

With respect to the alloys listed in Table 2-3 there are three common strengthening mechanisms: (i) solid solution hardening (Cr, Fe, Al, Nb, Ti, Mo); (ii) coherent precipitate hardening (mostly from Al, Ti or Nb additions) forming γ' and γ"; (iii) incoherent precipitate strengthening (carbide phases $M_{23}C_6$, M_6C and MC, where M is Cr, Fe, Nb, Ti and Mo). The contribution of each mechanism to the mechanical and creep strength of the Ni-alloys used in nuclear reactors is dependent on the various thermo-mechanical treatments that have been developed to suit the different applications [Strasser and Ford, 2012; Read, 2006].

For the precipitation-hardened alloys (like X-750 and 718) there is a wide range of properties that are sensitive to the size, number density and spatial distribution of the precipitates. Carbides typically form during high temperature heat treatments and are often segregated to grain boundaries [Strasser and Ford, 2012]. The γ' and γ"-coherent precipitates form within grains and also at grain boundaries (Figure 2-64). The intra-granular precipitates, in particular, impart an important strengthening

component; their size and density being controlled by aging treatments to give specific properties [Yonezawa, 2012; Strasser and Ford, 2012; Read, 2006; Smith and Patel, 2005]. In the over-aged condition these precipitates lose their ordered structure and evolve into the larger η and δ phases. The γ'-phase, in particular, is responsible for an important property of Ni super-alloys, i.e. high yield and creep strength up to high temperatures. For some alloys the yield strength actually increases with increasing temperature [Read, 2006], see Figure 2-59.

One popular explanation for the positive temperature dependence of the yield stress in some super-alloys is related to dislocation reactions that occur within the ordered γ' phase. Gliding dislocations of the type a/2<101>{11$\bar{1}$} sometimes act in pairs when cutting through γ' precipitates. The anti-phase boundary (APB) created by the passage of a single a/2<101> dislocation on {11$\bar{1}$} can be removed by the passage of a second "super-partial". The creation of the APB increases the critical resolved shear stress for that slip system by about 400 MPa [Read, 2006]. Passage of a second dislocation with the same Burgers' vector and slip plane removes the APB thus allowing a slip band to cut through the precipitates with reduced energy. The paired super-dislocations are either coupled strongly or weakly depending on the size and distribution of the γ' precipitates. For a/2<101>{11$\bar{1}$} dislocations cutting through an ordered γ' precipitate there is an increased propensity for cross-slip onto {010} planes, forming Kear–Wilsdorf locks [Kear & Wilsdorf, 1962], as the temperature is increased. At temperatures above that corresponding to the peak in the yield stress (about 800 °C) there is a preference for a/2<101> slip on the {010} plane and the γ' phase then acts like most other metal phases where softening occurs with increasing temperature [Beardmore et al., 1969], see Figure 2-59.

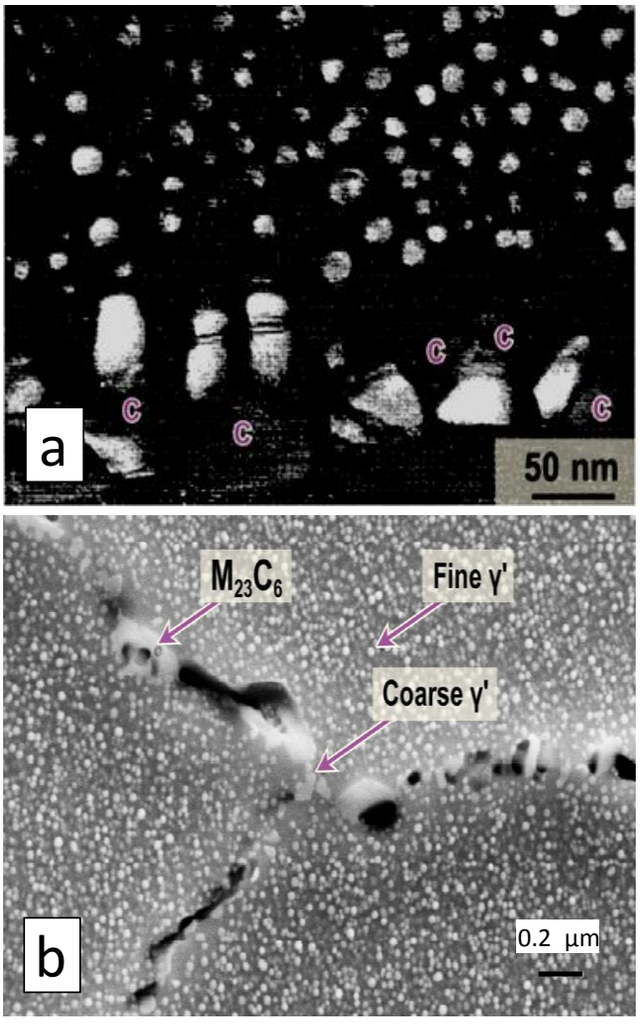

Figure 2-64: Micrographs showing the fine intragranular γ' precipitates and coarser γ' at the grain boundary together with intergranular carbides (labelled C in (a)) in Inconel X-750 after a HTH heat treatment. (a) Dark-field TEM micrograph adapted from Bajaj et al. [Bajaj et al., 1999]; (b) SEM micrograph supplied by P. Morra. Adapted and reproduced from Strasser and Ford [Strasser and Ford, 2012].

The Kear-Wilsdorf mechanism is only applicable to the mechanical properties of the alloy in cases where the γ' precipitates are cut by dislocations; this mechanism depends on the precipitate size, spatial distribution and volume fraction [Read, 2006]. Intra-granular precipitates harden materials by acting as barriers to dislocation slip. The dislocations can move through a material containing intra-granular precipitates by either cutting through, or by-passing, the precipitates (Orowan looping), see Figure 2-65. The tendency to cut or by-pass depends on the size and spacing of the precipitates.

Read [Read, 2006] has shown that, for a given volume fraction of γ' phase, the optimum hardening in the Ni-based super-alloys occurs for a particle size that lies at the transition from weak to strong coupling between the paired a/2<101>{11$\bar{1}$} super-dislocations that traverse the precipitates. For PE16, an optimum precipitate radius (r) was reported to be in the range 26–30 nm [Read, 2006], although lower values are found for other alloys like Inconel X-750 [Del Valle et al., 1998]. Precipitates larger than this optimum value are more likely to be by-passed by dislocations via the Orowan mechanism [Read, 2006]. Other theories of dislocation interactions with precipitates consider single dislocations only. For single dislocations the tendency to cut or by-pass a precipitate depends on the dislocation line tension, which is a function of the radius of curvature of the dislocation line. By considering the line tension, Brown has shown that cutting tends to occur when precipitates sizes are small and Orowan looping tends to be observed when precipitates are large [Brown, 1979]. For the condition where Orowan looping dominates, the strengthening is determined by both precipitate size and spacing considerations as outlined by Bacon et al. [Bacon et al., 1973].

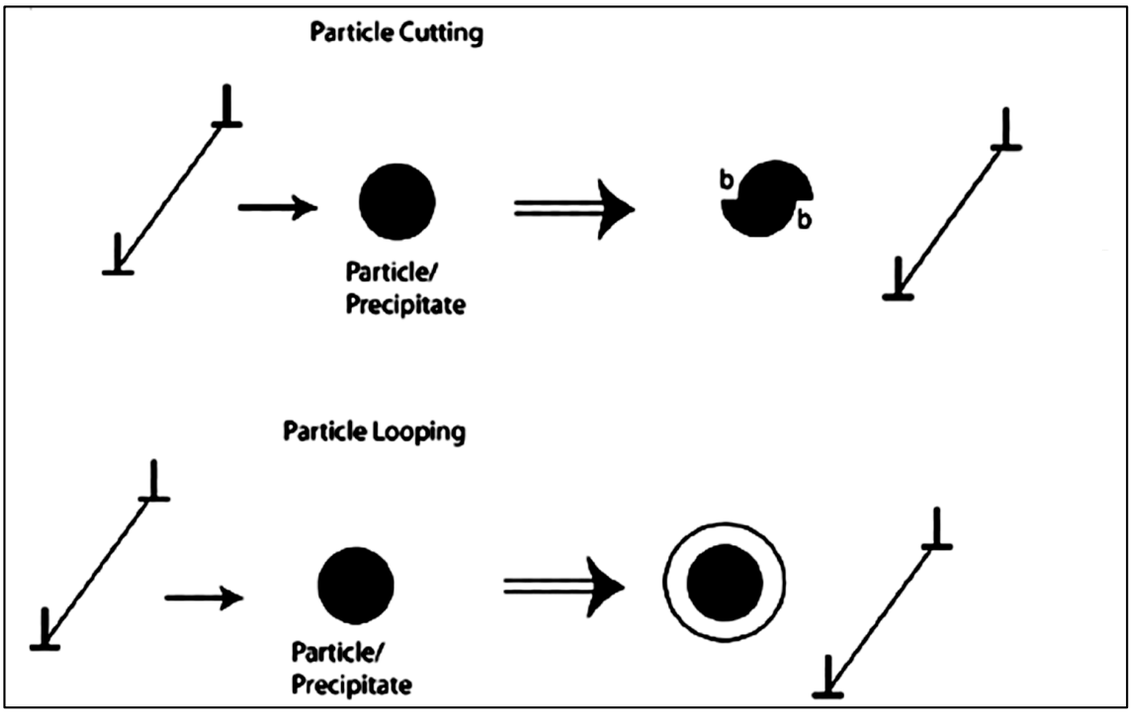

Figure 2-65: Schematic diagrams illustrating the interactions of edge dislocations (Burgers' vector = b) with intra-granular precipitates. Both cutting and looping hinder the dislocation motion resulting in an increased yield stress. The tendency for either mechanism is dependent on the precipitate size and spacing (see text).

Although Del Valle et al. [Del Valle et al., 2001] concluded that for Inconel X-750 the optimum radius for precipitate strengthening, and therefore the transition from precipitate cutting to Orowan looping, was about 15 nm, they also reported instances where this was not the case [Del Valle et al., 1998; Del Valle et al., 2001].

The mechanical properties of Ni-alloys are largely dependent on solution strengthening, grain size refinement (controlled to some extent by heat-treatments to form grain boundary carbides) and precipitation strengthening (primarily γ' and γ''). There are many thermo-mechanical process routes to tailor the properties for different applications and these are described in each of the pertinent technical specifications [Special Metals Corporation, 2019]. The alloying elements responsible for the

γ and γ' phase formation are Ti, Al, Nb and Ta (Figure 2-61). Alloys with appreciable concentrations of these elements are said to be precipitation-hardenable, e.g. Inconel X-750, 718, 706. Alloys with low concentrations of the γ and γ' phase forming elements, e.g. Inconel 600 and 690 are solution-strengthened only. The tensile properties of typical precipitation-hardened (alloy 706) are compared with a solution-treated alloy (alloy 600) in Figure 2-66. It is clear that the precipitation-hardened alloy (706) has a higher strength but less ductility than the solution-annealed alloy (600).

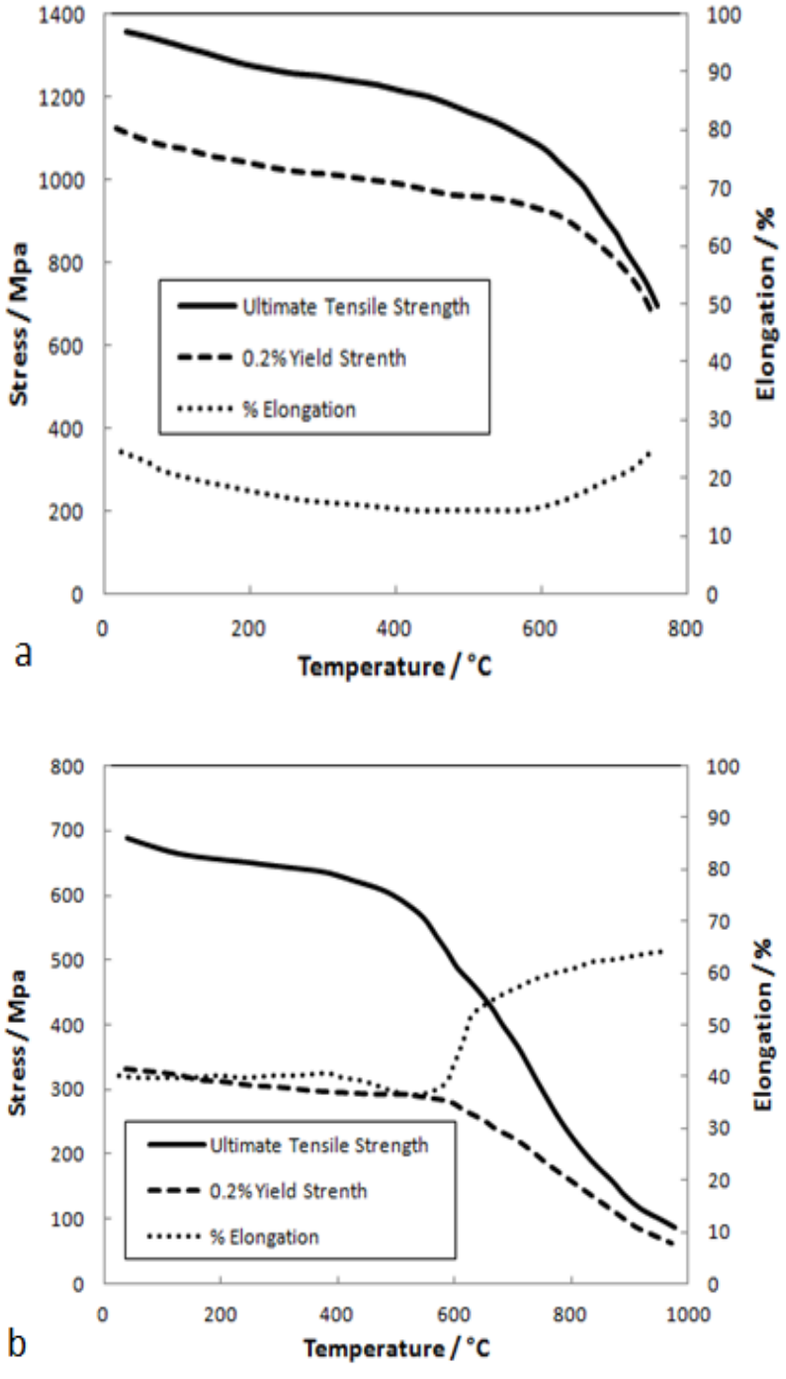

Figure 2-66: Tensile properties as a function of temperature for: (a) Inconel 706. Solution treatment at 1700-1850°F (925-1010 °C) for a time commensurate with sample size, air cool. Precipitation treatment at 1350°F (730 °C) for 8 hr, furnace cool at 100 °F (55 °C) per hour to 1150 °F (620 °C) for 8 hours and the air cooled; (b) Inconel 600. Annealed at 1600 °F (870 °C) for 1 hour and then hot-rolled. [Special Metals Corporation, 2019].

2.3.5 Mechanical Properties during Irradiation

2.3.5.1 Fast Reactor and Ion Irradiation Facilities

Ni-based alloys can be categorised into two classes: solution-annealed (SA), comprised of a single face-centred-cubic austenitic phase, and aged or precipitation-harden-annealed (PHA), comprised of ordered Ɣ' or Ɣ'' precipitates in an austenitic matrix. The response to neutron irradiation is markedly different. Mechanical test results from Byun and Farrell [Byun and Farrell, 2003] on SA and PHA materials Irradiated in the HFIR reactor at 60 °C – 100 °C are summarised in Figure 2-67. At these low temperatures and doses up to 1.2 dpa the PHA material exhibits reduced ductility but little hardening with increasing dose, whereas the SA material exhibits marked irradiation-hardening in addition to a reduction in ductility.

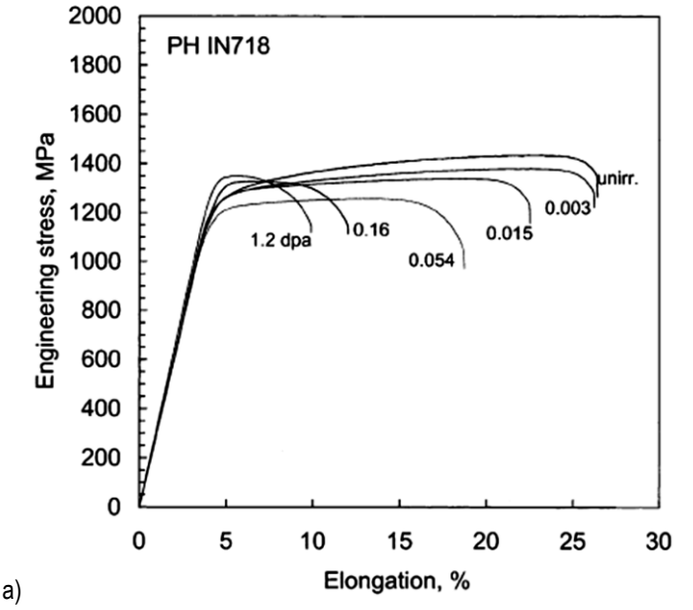

a)

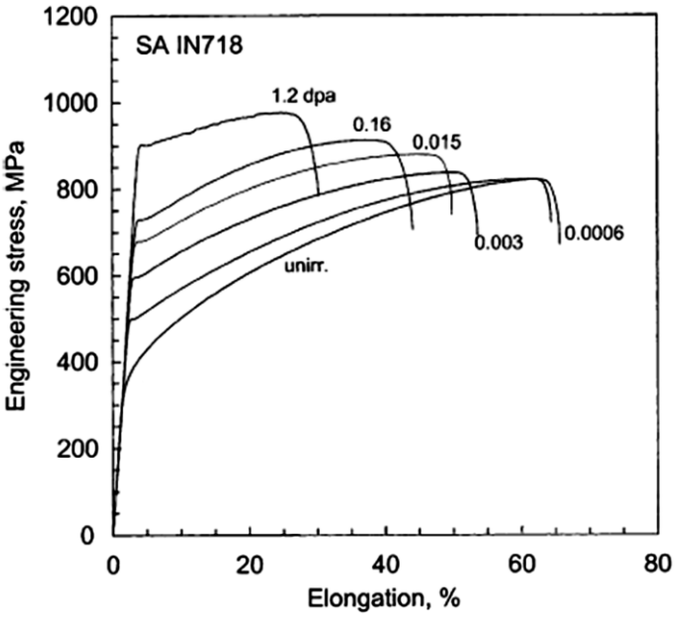

b)

Figure 2-67: Engineering stress–strain curves of: (a) precipitation-hardened IN718, and (b) solution-annealed IN718 at a temperature of 60 °C – 100 °C to various doses [Byun and Farrell, 2003].

Work by [Hunn et al., 2001] on H, He and 3.5 MeV Fe-ion irradiation of Inconel 718 at 200 °C showed that after an initial transient increase in hardness at low doses (< 1 dpa), softening of precipitation-hardened material occurred at increasingly higher doses. Softening (lower yield strength) was exhibited by precipitation-hardened Inconel 718 at high doses (>10 dpa) but not for the same material in a solution-annealed state, Figure 2-68.

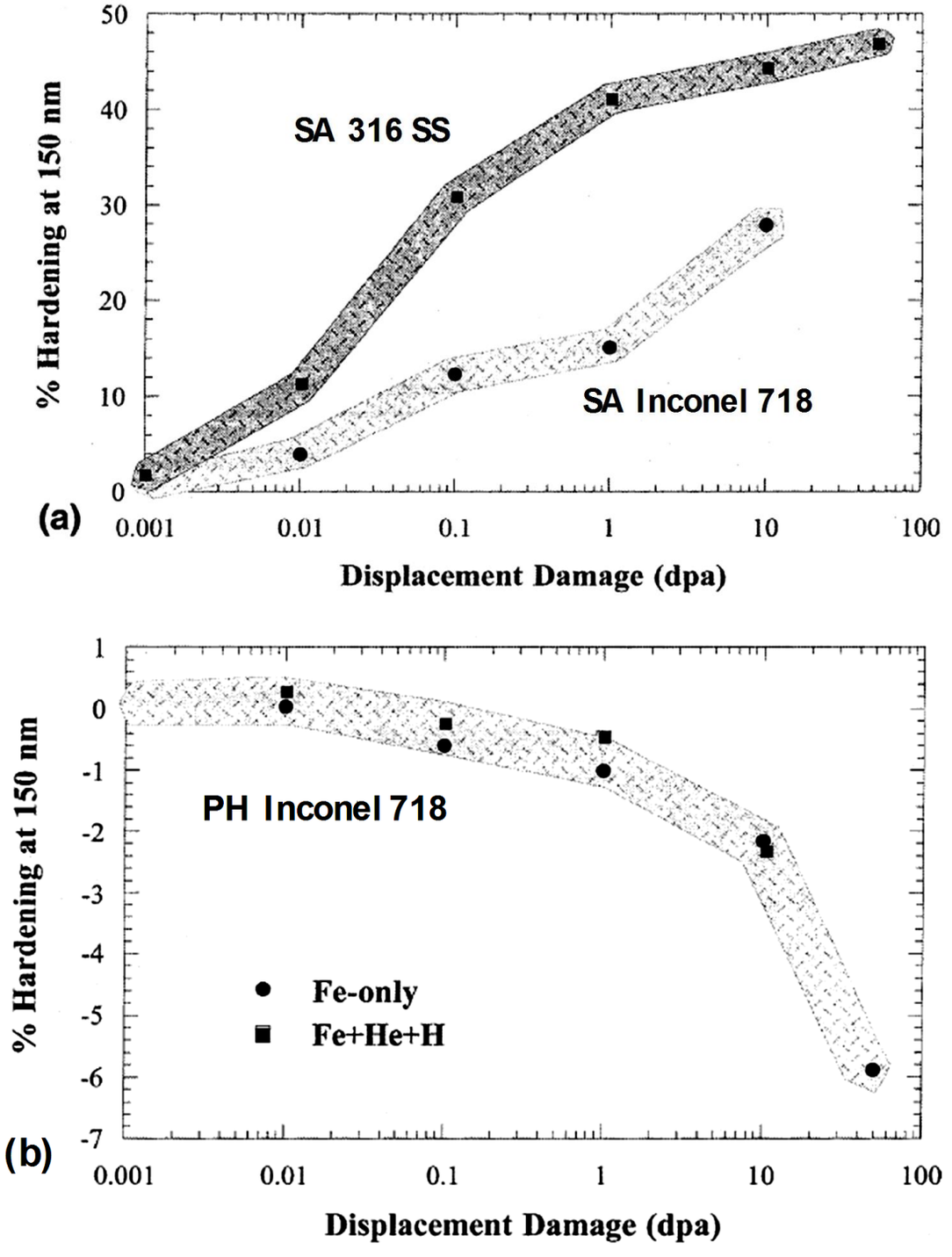

Figure 2-68: Relative indentation hardness of: (a) solution-annealed IN718, and (b) precipitation-hardened IN718 irradiated at 200 °C to various doses [Hunn et al., 2001].

Given the severe reduction in ductility (Figure 2-70(a)) and the inter-granular nature of the failure at high doses (Figure 2-71(b)) one must consider the possibility that He embrittlement is occurring. Although no details of the He generation in the window material were given it is likely that the He generation per dpa would be comparable with the water degrader window (about 150 appm/dpa [James et al., 2001]) and therefore He concentrations are likely to be about 3000 appm He for the window at 20 dpa. The (p,α) reactions at the centre of the beam striking the water degrader produced He at a concentration of about 1400 appm, corresponding with about 10 dpa [Hamilton et al., 2000; Carsughi et al., 1999]. Hydrogen generation are about two times higher [James et al., 2001].

2.3.5.2 Light Water Reactors

The combination of high strength and corrosion resistance has led to Ni-alloys being widely used in BWRs and PWRs for reactor internal structural applications including fuel assembly hold-down springs, control rod guide tube support pins, jet pump beams, tie-rods and core internal bolting. Some of the Ni-alloy reactor components subjected to high stresses during service have experienced premature failures, mostly linked to SCC [Strasser and Ford, 2012].

Work on the performance of Ni-alloys in BWR and PWR environments has primarily focused on SCC and IASCC. One such study involved testing of internally stressed tubes made from Inconel 625, X-750 and 718 in test assemblies inserted in operating PWR and BWR reactors [Garzarolli et al., 1985, 1987, 1993]. The results of these tests demonstrated the propensity for SCC failure of these alloys with different metallurgical states compared with some stainless steels. Garzarolli et al., [Garzarolli et al., 1987] concluded that “Inconel 718 with the proper heat treatment and high purity AISI 348 behaved well in the environments studied”.

TEM examinations and hardness testing on the Inconel 718 irradiated with neutrons at 288 °C from the Garzarolli study [Garzarolli et al., 1985] has provided information on the changes on the γ’ and γ’’ precipitate structure related to the changes in yield strength [Thomas and Bruemmer, 1997; Thomas et al., 2001]. Thomas and Bruemmer [Thomas and Bruemmer, 1997] showed that the hardness of Inconel 718 after 3.5 dpa at 288 °C was similar to the unirradiated state and there was marked softening for a dose of 20 dpa (Figure 2-72). They showed that the γ’ precipitates disordered at low doses and both the γ’ and γ’’ precipitates dissolved and dispersed with increasing dose (Figure 2-73). As disordering was complete at doses < 1 dpa, it is then clear that the softening with increasing dose (up to 20 dpa) can be related to the dissolution and dispersion of the precipitates rather than any effect of disordering. Qualitatively similar results were obtained at lower neutron irradiation temperatures in Inconel 718 by Byun and Farrell [Byun and Farrell, 2003]. Byun and Farrell observed progressive irradiation hardening in solution annealed Inconel 718 over a dose range up to 1 dpa. Precipitation hardened Inconel 718 showed little change in yield strength and some reduction in ultimate tensile strength up to 1 dpa.

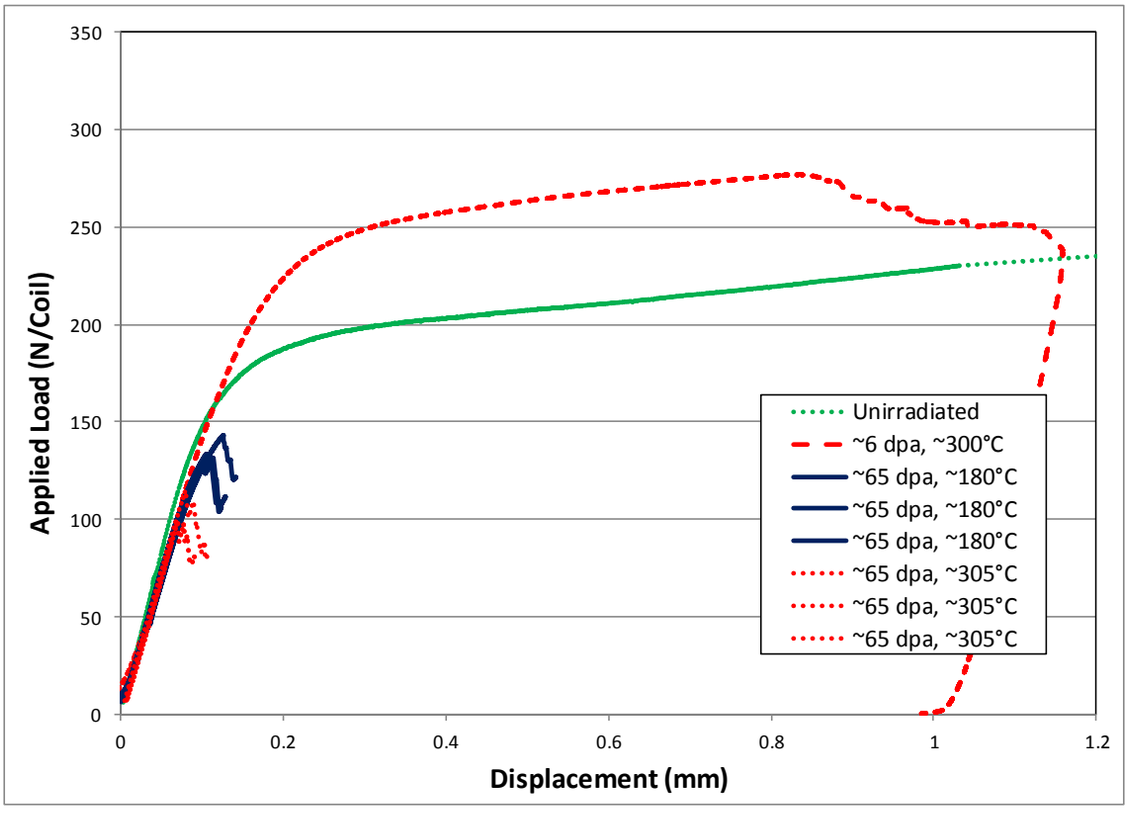

Figure 2-75: Load-displacement curves at room temperature for Inconel X-750 as a function of irradiation temperature and displacement damage dose (dpa). The He/dpa ratio is approximately 300 appm He/dpa. [Modified from C. Howard et al., 2015].

The behaviour of the Inconel X-750 spring material can be understood from an examination of the microstructure. The microstructure evolution in Ni-base alloys during irradiation is very sensitive to the interstitial and vacancy mobility that is governed primarily by the temperature. The microstructure is also profoundly affected by the presence of insoluble gases, in particular He, produced by transmutation. There are three main features of the microstructure that are affected by irradiation: cavities, dislocations and precipitates (second phases).

2.3.6 Irradiation Microstructure

2.3.6.1 Cavities

The microstructure evolution of Ni-base alloys in power reactors is largely dictated by the initial microstructure and transmutations producing He and H. Although He generation is the main driver for the cavity formation, the growth of cavities is dictated by the irradiation temperature and damage rate (neutron flux) [Golubov et al., 2012]. For Ni- alloys and steels at power reactor operating temperatures the growth of cavities, and therefore the swelling, is very sensitive to the temperature. The temperature dependence of swelling (and also creep) is non-linear over the temperature range where there is a transition from recombination-dominated to sink-dominated point defect reaction kinetics. For a vacancy migration energy of 1.38 eV the transition from recombination-dominated to sink-dominated regimes occurs between 200 °C and 300 °C for the damage rates and sink densities that apply to common engineering alloys in LWRs [Griffiths, 2019], (see section 4.3). The lower freely-migrating point defect flux at the lower irradiation temperature reduces the rate of irradiation damage evolution because of increased recombination. The volume swelling from cavities formed at reactor operating temperatures corresponds approximately to He/V = 1 [Judge et al., 2016] indicating that the cavities produced at these low temperatures can be classed as bubbles, as opposed to voids. There are few data available showing the cavity microstructure in Ni-alloys in PWR reactors. Austenitic steels are likely to have a similar irradiation damage response because they are austenitic

alloys with an FCC crystal structure and have vacancy migration energies that are very similar [Griffiths, 2019; Griffiths et al., 2017]. Cavities in 316 stainless steel irradiated in a PWR are similar in size to those found in CANDU power reactors [Edwards et al., 2009; Judge et al., 2016]. Cavities in Inconel X-750 irradiated in a CANDU reactor are illustrated in Figure 2-76. For stainless steels and Ni-alloys irradiated in power reactor cores the cavities are small and are high in density. Higher densities and larger cavities are observed on grain boundaries compared with the matrix (Figure 2-77), this being a characteristic of He-stabilised cavities [Griffiths, 2019].

Although He generation is the main driver for the cavity formation, the smaller point defect clusters at the lower temperature can be understood based on conventional considerations of the effect of temperature on cluster formation and growth [Griffiths et al., 2017]. For a vacancy migration energy of 1.38 eV the transition from recombination-dominated to sink-dominated regimes occurs between 200 °C and 300 °C for the applicable damage rates and sink densities [Golubov et al., 2012]. The cavity size in the matrix is smaller and has a higher density at the lower temperature, Figure 2-76. A similar difference due to irradiation temperature is observed for cavities segregated at grain boundaries, Figure 2-77 [Judge et al., 2016]. In the latter case there is a clear increase in the density of cavities on the grain boundaries at both low and high temperatures. The volume swelling from cavities formed at reactor operating temperatures corresponds approximately to He/V = 1 [Judge et al., 2016] indicating that the cavities produced at these low temperatures can be classed as bubbles, as opposed to voids.

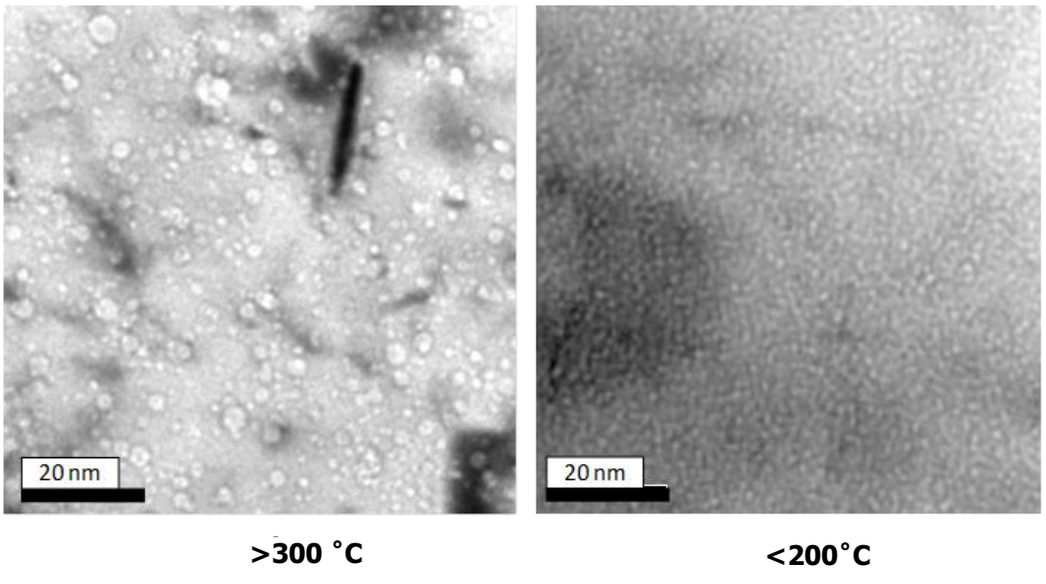

Figure 2-76: TEM micrographs showing cavity structure in Inconel X-750 material after irradiation to about 55 dpa /18000 appm He at about 300 °C and 45 dpa /15000 appm He at about 200 °C, [Griffiths, 2014].

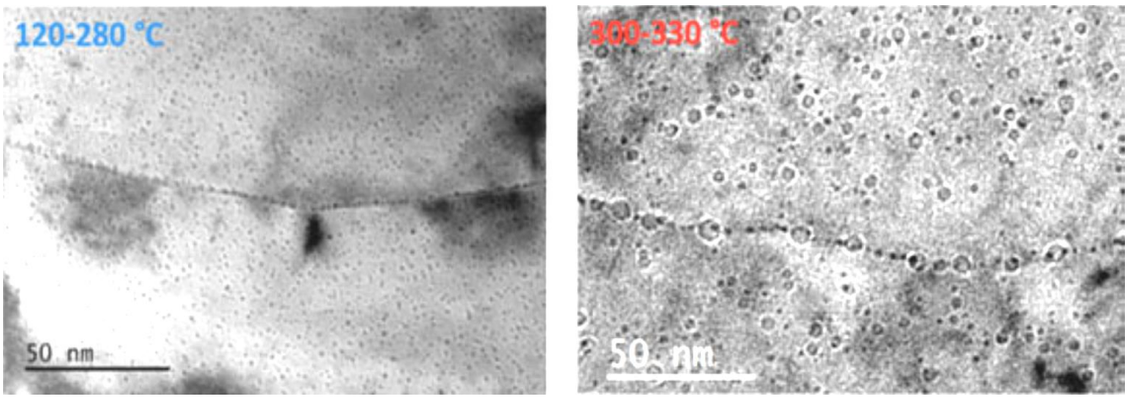

Figure 2-77: TEM micrographs showing cavity structure in Inconel X-750 after irradiation to about 70 dpa and about 22 000 appm He at low temperatures (about 200 °C) and high temperatures (> 300 °C), [Judge et al., 2016].

The cavities that are produced at low temperatures are stabilised by insoluble He. Perhaps one of the more intriguing aspects of cavity evolution observed in all austenitic alloys in fast reactors and ion or electron irradiations is the fact that cavities exist in the absence of high concentrations of insoluble gases such as He [Brailsford and Bullough, 1972]. In such circumstances the cavities may be classed as voids, i.e. they contain no gas. Void formation in the absence of a stabilising gas is hard to understand given that the most energetically stable state for a small vacancy cluster is a dislocation loop, irrespective of whether the void has a low surface energy, which is a driver for the collapse in the absence of an internal pressure. Vacancy loops are biased sinks for self-interstitial atoms thus effectively promoting recombination. One would therefore expect that void growth (swelling) is strongly dependent on the stabilisation of small vacancy clusters. Bias-driven growth of voids may be expected in the presence of a high biased interstitial sink strength (high dislocation density) once the voids exceed a certain size. The conundrum regarding void formation in the absence of a stabilising insoluble gas has been discussed by Brailsford and Bullough [Brailsford and Bullough, 1972]. They noted that voids were often stabilised on incoherent precipitates such as the many carbides that often exist in austenitic alloys, but not coherent precipitates, such as Ɣ', and concluded that "…an incoherent precipitate has an unrestricted capacity for point defects and hence plays a role analogous to an isolated void, whereas a coherent precipitate has only a finite capacity for point defects and simply augments intrinsic recombination".

There is a dearth of observations on cavities at power reactor operating temperatures (about 300 °C) as noted by Rowcliffe et al. [Rowcliffe et al., 2009]. Boothby [Boothby, 2012] also noted that at low temperatures there was a dearth of data concerning He bubbles on boundaries and this absence was probably related to the fact that the bubbles were likely small (< 1-2 nm in diameter). This observation could be because of the high vacancy migration energy of Ni (about 1.4 eV) limiting cavity growth due to the absorption of excess vacancies created by irradiation damage [Griffiths, 2014; Griffiths, 2019; Griffiths et al., 2017], the low temperature behaviour (<300 °C) is therefore dominated by point defect recombination (see Section 4.3). Because there are few observations of cavities at low temperatures void swelling and He embrittlement have generally not been considered a concern in the past [Rowcliffe et al., 2009]. Given that cavities with diameters about 1nm are at the limit of resolution for many older microscopes, it is likely that they were simply not observed in many of the early studies. It is only since 2009 that observations of cavities at grain boundaries have been made for stainless steel components [Edwards et al., 2009] and Ni-based alloys [Griffiths, 2014; Griffiths, 2019; Judge et al., 2016] removed from power reactors.

2.3.6.2 Dislocations

At power reactor operating temperatures, the irradiation damage clusters in the form of dislocation loops in Ni-alloys are generally low in density and small in size [Griffiths, 2014; Zhang et al., 2014]. Bright field TEM images show that the dislocation structure is cleaner (fewer, or smaller, or both point defect clusters) at lower compared with higher irradiation temperatures, Figure 2-78.

The lower freely-migrating point defect flux at the lower irradiation temperature reduces the rate of irradiation damage evolution because of increased recombination and may be responsible for the apparent lower damage cluster density shown in Figure 2-78 that does not depend on He. Transmission electron microscope (TEM) observations show that the network dislocation structure is relatively clean at the lower temperature, but is decorated by point defect clusters at the higher temperature, indicating that the lower temperature corresponds to the recombination-dominated regime for point defects [Zhang et al., 2014].

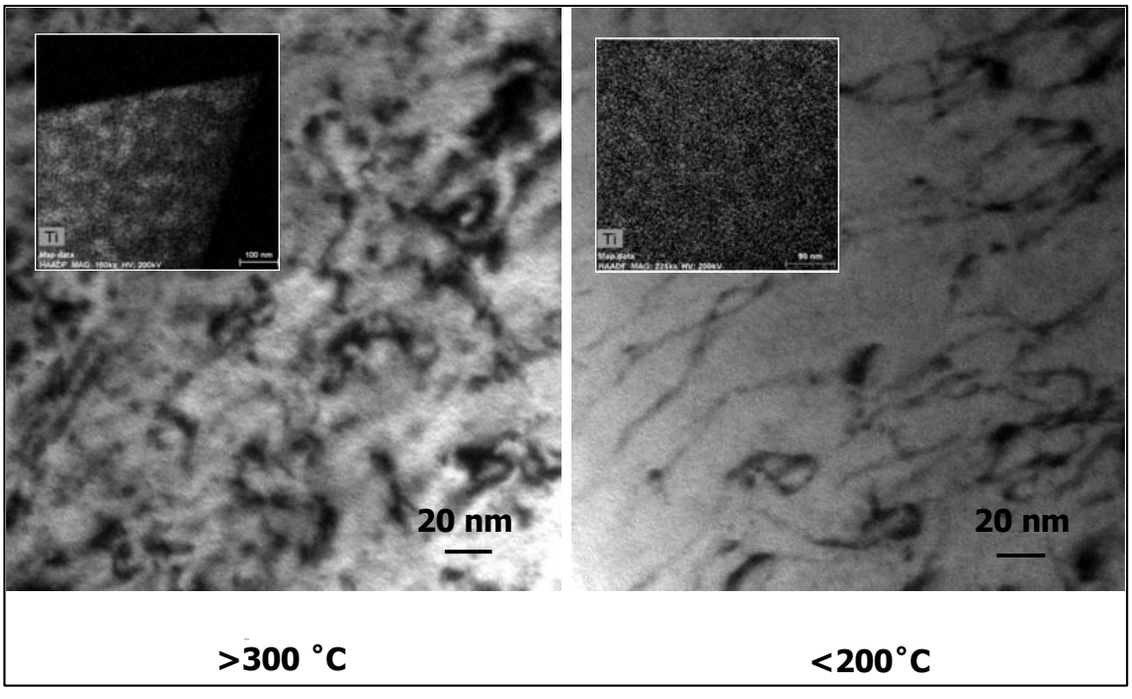

Figure 2-78: TEM micrographs showing dislocation structure in Inconel X-750 material after irradiation to about 55 dpa and 18000 appm He at about 300 °C and 200 °C; diffracting vector = 220, [Zhang et al., 2014]. Insets provided by Z. Yao, Queens University, with permission.

2.3.6.3 Precipitates

The insets in Figure 2-78 show that the Ɣ' precipitates, which are dissolved or dispersed during irradiation, are diffuse after irradiation at the lower temperature, consistent with the results of Nelson et al. [Nelson et al., 1972]. There is also a temperature dependence on the disordering of the Ɣ' during irradiation with a higher degree of disorder at lower temperatures [Judge et al., 2016]. Using parameters applicable to Ni-based alloys, such as PE16, Nelson et al. [Nelson et al., 1972] showed that, for a displacement damage rate of 10^{-6} dpa.s^{-1}, the steady-state radius of Ɣ' precipitates was vanishingly small at 200 °C, but was between 20 nm and 120 nm at 300 °C, depending on the initial precipitate density. They argued that the dissolution and dispersion of the Ɣ' precipitates were a balance between irradiation-induced mixing and a diffusional-driven transformation back to the quasi-equilibrium state. Nelson et al. [Nelson et al., 1972] deduced that there was a critical temperature for a given damage rate above which diffusion would start to dominate and reform the dispersed precipitates. At this critical temperature the irradiation-enhanced diffusion coefficient would be just sufficient to allow the diffusion of solute atoms to re-form the precipitate to balance the loss by irradiation-induced dissolution. For a damage rate of 10^{-6} dpa.s^{-1} their calculations showed that this critical temperature was somewhere between 200 °C and 300 °C, which is consistent with observations after ion irradiation.

2.3.7 Discussion

Unlike Zr-alloys and stainless steels the mechanical properties of Ni-alloys can be complex because of the nature of the precipitates in precipitation-hardened material and because of the unique response to irradiation resulting in large amounts of He production. The effect of the γ' precipitates on the anomalous temperature dependence of yield strength is only observed when the volume fraction of the γ' is high. For most engineering components these super-alloy characteristics of Ni-alloys are not manifested in reactor operation and the irradiation effects on superalloy properties have not been studied. The disordering of the γ' precipitates will soften the material but the softening effect due to disordering is only realised in the early stages of irradiation when other changes in the microstructure are also occurring. Consequently, most Ni-alloys exhibit an increase in strength at low doses that can be attributed to the hardening effect of irradiation damage clusters (dislocation loops and cavities).

3 Mechanical property testing of archive and irradiated zirconium alloy components

3.1 Introduction

Mechanical testing of zirconium alloys has many uses such as:

- to confirm that the material meets the specification,
- to evaluate new alloys or modifications to old ones,
- to elucidate mechanisms of strengthening or embrittlement, and
- to assess the effects of reactor operation.

The mechanical response of any material depends on several different parameters such as:

- Specimen geometry,
- Alloy composition and microstructure,
- Loading conditions such as stress state and strain rate, and
- Environment such as temperature, irradiation and ambient chemistry.

Residence in a nuclear reactor presents a severe test for materials. Before evaluating the mechanical properties, knowledge is required on the conditions of normal reactor service with its operational variations, the challenge when spent fuel is stored, and the consequences of accidents. Various mechanical tests are done to simulate the conditions faced by fuel cladding and structural components in the reactor. In applying the results from mechanical testing of zirconium alloys to reactor performance, it is crucial to have a good knowledge of the situation being addressed and how the different critical testing parameters affect the material response so the results are useful to predict performance accurately and satisfy regulatory requirements. The objective of this section of the STR is to provide this knowledge. Background information will be included where appropriate, but an extensive literature review of specific performance is not intended.

In most applications, in-reactor mechanical behaviour can be determined by proper out-of-reactor testing of irradiated material, but not of unirradiated material. Unirradiated archive material is also tested for comparison of the measured unirradiated and irradiated material properties to evaluate the effects of irradiation and reactor chemistry. A number of various types of tests can be performed such as:

- Hardness testing
- Tensile testing
- Creep testing
- Burst testing
- Fatigue and fatigue crack propagation testing
- Fracture toughness testing
- Delayed hydride cracking

We will limit our focus in this STR to the standard properties that one would determine from a tensile test or in a fracture toughness test. Most of the information provided in this section was presented in ZIRAT18 [Adamson et al., 2013a].

3.2 Tensile testing

Tensile testing to obtain mechanical properties of zirconium alloy components is essential to understanding reactor component behaviour and to insure safe reactor operation. Although due to the nature of test data needed (unique component geometry and radioactivity of the materials) many test techniques used in the industry are not “standard”, several ASTM International Standard Practice documents are useful and applicable:

- E8/E8M- Test methods for Tension Testing of Metallic Materials
- E83- Practice for Verification and Classification of Extensometer Systems
- E21- Standard Tests Methods of Elevated Temperature Tension Tests of Metallic Materials
- E6- Standard Terminology Relating to Methods of Mechanical Testing

Since ASTM standard tensile testing cannot be performed in most cases due to size limitations of the Zr alloy component, careful choice of specimen design is needed to insure tests simulate the stress-strain-environment of the component of interest. For irradiated material, it is important to account for highly localized deformation when determining, for example, failure strain on a specimen that does not represent component geometry, or stress state.

When preparing to perform tensile testing of a material or component of interest, several factors must be considered:

- Careful analysis of the intended application of the data
- Material availability
  - Irradiated or not
  - Actual component or not
- Means of fabricating specimen
- Conditions to be simulated (represented or “mocked-up”)
  - Temperature
  - Strain rate
  - Stress state
  - Stress or displacement-controlled deformation
  - Environment
- Specimen geometry
  - Plane strain
  - Plane stress
  - Gauge length and gauge shape
- Metallurgical condition of material
  - Irradiated or not
  - Crystallographic texture
  - Heat treatment (recrystallized, (RX), partial recrystallized (PRX), cold-worked (CW), cold-worked and stress-relieved (CWSR), quenched (Q) or quenched and aged (QA)
  - Hydrided or not
- Test facility
  - Allow radioactivity or not (exposure value from the test sample)
  - Apply and measure force and displacement

- Measure or calculate strain
- Post-test examinations

3.2.1 Tensile testing equipment

Although coming in many forms, the workhorse tensile test machine is the closed-loop servo hydraulic system shown schematically in Figure 3-1. Heavy-duty screws mechanically drive older systems, not shown, while the illustrated system uses an oil-pressurized piston. The screwdriver machines have the advantage of providing a controllable and steady motion, while the servo hydraulic machines are able to provide variations in load or movement patterns.

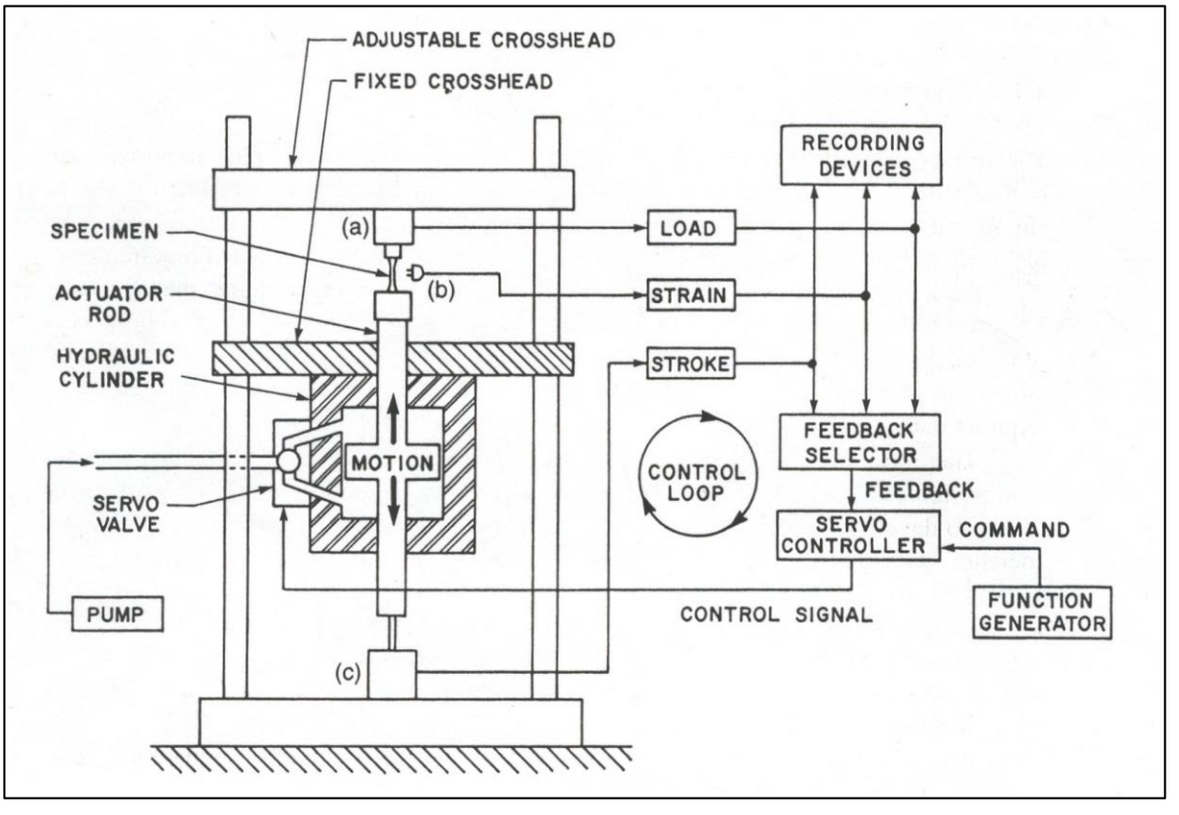

Figure 3-1: Modern closed-loop servo hydraulic testing system, schematic diagram after [Dowling, 1999].

Typically the three employed sensors include (a) load cell, (b) extensometer, and (c) linear variable differential transformer (LVDT.) Applied force or load is measured by a load cell and elongation of the specimen is obtained either by an extensometer attached or focused on the specimen gauge, or by electronically monitoring the motion of the machine crosshead. In the latter case, the moving parts of the loading system must be rigid or stiff enough to ensure all measured motion can be attributed to the specimen. In the former case, extensometers include LVDTs, strain gauges, and non-contact laser devices.

The test specimen is attached to the loading or straining system by some form of grips. ASTM Standard E8/E8M recommends standard grips, but often special grips must be designed to fit the specimen design, to be discussed later. Grips and load-bearing components are made of high strength-creep resistant alloys such as 17-4PH stainless steel, MarM247C [Alam & Hellwig, 2009] or when testing for pellet-clad interaction (PCI) and stress corrosion cracking (SCC) environments, a molybdenum alloy is used [Coffin, 1979].

Strain rate on the specimen during the test can be important. Normally strain rates are in the range $3x10^{-5}$ s^{-1} (slow) to $1x10^{-3}$ s^{-1} (fast). For reference, to obtain 5% strain at a rate of $5x10^{-4}$ s^{-1} would take about 100 seconds.

Under normal reactor conditions zirconium alloy components operate in the broad temperature range 270 °C (543 K) to 375 °C (648 K). During shutdowns or handling in the storage pool the temperatures approach but are generally above "room" temperature, loosely defined here as 30 °C (303 K). This entire range of specimen temperatures can be easily attained by heating systems, including clamshell incandescent heaters, by induction coils around the specimen or by electrical resistance heating through the specimen. Since testing times are short, testing in air is normally satisfactory. Temperature measurement is usually accomplished by thermocouples attached to the specimen or grips, or in rare cases by infrared temperature monitors.

Annealing irradiation-damage in zirconium alloys begins at about 350 °C (623 K) and becomes rapid at 400 °C (673 K). For a review see Section 5 of ZIRAT17/IZNA12 Annual Report [Rudling et al., 2012].

3.2.2 Test material

The source of material and specimens for testing is generally the reactor components themselves, e.g., tubing and flat products of various sizes. Table 3-1 gives a sample of dimensions for typical components [Adamson et al., 2013a]. It is seen that for BWRs and PWRs, dimensions are small and often are not suitable for fabricating standard specimen geometries. The same is true for CANDU components, although thickness and diameter of pressure tubes are larger than those of fuel cladding.

Table 3-1: Typical dimensions of reactor components (approximately only; not design specifications; varies with bundle design) [Adamson et al., 2013a].

	Thickness, mm	Outside diameter, mm
BWR clad	0.6	10
PWR clad	0.6	9.5
BWR water rod	0.8	20
PWR/BWR spacer/grids	0.5	Sheet
BWR channel	2.5	Plate
CANDU clad	0.4	12
CANDU calandria tube	1.4	132
CANDU pressure tube	4.2	100
		© ANT International 2013

The other complication is that materials from the reactor are radioactive, and specimen fabrication must be done in a controlled area or hot cell. This process is readily accomplished using standard techniques:

- Remote milling using a pre-programmed computer-controlled milling machine located in-cell with the operator out-of-cell.
- Standard electro-discharge machining (EDM) conducted in cell [Coleman et al., 1972] or, for low dose rate material, in a controlled laboratory.

Before testing, fuel must be removed from fuel rods. A dual chemical and mechanical process usually achieves this preparation. Great care must be taken not to damage the inner rod surface, as future mechanical testing may be compromised.

It is important when conducting laboratory or hot cell testing to stress the specimen in an appropriate direction. For examples, cladding tubes are invariably stressed in the circumferential (hoop) direction by the expanding fuel and PWR guide tubes are often stressed in the axial direction by forces from grids during the complicated dimensional instability of the guide tube assembly. In addition, plane strain conditions are often imposed on cladding deformation during power transients. Plane strain

4 Deformation Mechanisms and Irradiation Effects

The mechanical properties of metal alloys are largely dependent on the force need to shear the material by the creation and movement of dislocations and twins. In addition to the intrinsic properties of the single crystal structure, the deformation is affected by solute atoms, precipitates, grain structure and texture. Irradiation results in changes in the microstructure that can either increase the strength of the material by the creation of barriers to slip (point defect clusters such as cavities, precipitates and dislocation loops) or decrease the strength by the disordering and dissolution of incoherent and coherent hardening phases. The microstructure evolution during irradiation is a function of the atomic displacement dose, dose-rate and temperature. Dose-rate effects on microstructure evolution can be significant by promoting point defect recombination but may also have an effect on cluster density. Dose-rate effects are often confounded with spectral effects, especially when the neutron exposure is represented as a neutron fluence (flux x time) for a given energy range, e.g. E > 1 MeV.

4.1 Irradiation Damage Production

Irradiation of metal alloy components in a nuclear reactor results in damage to the material by atomic displacement. Gases such as He, in particular, are created from (n,α) reactions. Most atomic displacement damage is produced by neutrons with sufficient energy to displace individual atoms. For a direct head-on collision, the minimum energy to displace a Ni atom is about 600 eV and the minimum energy to displace a Zr atom is about 900 eV. Atomic displacements can also be produced from nuclear reactions involving particle or photon emission. Atomic displacement damage is produced by the energetic particle itself but is mostly the result of the recoil of the emitting atom. For elements such as Fe, Cr and Ni, used in many common engineering alloys, the (n,γ) reaction has a large reaction cross-section over a large range of thermal neutron energies. High energy (n,p) and (n,α) reactions may be important if there are sufficient high energy neutrons. Databases such as those freely available from the Los Alamos National laboratory [the LANL ENDF/B-xx nuclear library, http://t2.lanl.gov/nis/data.shtml] include cross-sections for atomic displacements. The cross-sections have units of barns (10^{-24} cm^2). When multiplied by the neutron fluxes for corresponding energy ranges the product with the atomic displacement cross-section is the atomic displacement rate, expressed as displacements per atom per second (dpa.s^{-1}). All possible nuclear reactions that can transfer energy to a target atom are included in codes such as SPECTER [Greenwood and Smither, 1985]. The atomic displacements are calculated from elastic and inelastic hard sphere collisions and also nuclear reactions involving neutron absorption and particle or photon emission.

For a hard-sphere collision, the calculation of the average energy transferred to the PKA from direct collisions with neutrons with a specific energy has to account for the probabilities of different scattering angles and the associated momentum transfer. If one considers that the cross section for a neutron of energy (E) producing a PKA of energy (T) is represented by σ(E, T) then the damage production can be determined by multiplying by a displacement function, $\nu(T)$, that is derived considering the energy available to create displacements and the minimum energy required to displace an atom (E_d), see [Norgett et al., 1975]. Cross sections are often determined on a per-atom basis (the probability of a reaction for any given atom), the number of displacements are then represented by displacements per atom (dpa). For a given PKA energy (T) only a portion of the energy contributes to atomic displacements in the collision cascade; this is called the damage energy. For neutron scattering events the total displacement damage is given by:

Equation 4-1:

$$Displacement\ Rate = \int_{E_d/\Lambda}^{E_M} \int_{E_d}^{\Lambda E_i} \varphi(E_i)\sigma(E_i, T)\nu(T)dTdE_i$$

where E_M is the maximum energy of the neutrons being considered,

E_d is the threshold displacement energy,

$\varphi(E_i)$ is the neutron flux with energy E_i,

$\sigma(E_i, T)$ is the cross section for a neutron with energy E_i to produce a recoil atom with energy T,

$\nu(T)$ is the displacement function for the PKA.

For non-fission neutron absorption and particle emission leading to a recoil of energy E_R, the number of displaced atoms due to the recoil is determined from the recoil energy using the same displacement function $\nu(E)$. The expression for displacement rate then becomes:

Equation 4-2:

$$Displacement\ Rate = \int_0^{E_M} \varphi(E_i)\sigma(E_i, E_R)\nu(E_R)dE_i$$

where E_R is the atomic recoil energy for a given reaction with that characteristic recoil energy.

The displacement function $\nu(T)$, or $\nu(E_R)$, depends on the threshold atomic displacement energy and includes energy lost (Q) by the PKA as a result of processes other than displacements,

$\nu(T) = 0$ when $T<E_d$

$\nu(T) = 1$ when $E_d<T<2E_d$

$\nu(T) = \kappa(T-Q)/2E_d$ when $T>2E_d$

where κ is the displacement efficiency, equal to approximately 0.8 [Norgett et al., 1975].

In practice $\sigma(E_i, T)$ and $\sigma(E_i, E_R)$ are not explicitly calculated in codes, such as NJOY [Macfarlane et al., 1984] and SPECTER [Greenwood and Smither, 1985] that use cross section data from various libraries, such as ENDF/B-V, to determine atomic displacement damage for neutrons of a given energy, E_i. Instead, such codes use available reaction cross sections for elastic and inelastic scattering, together with angular scattering data and models for both resolved and unresolved nuclear excitations, and reaction cross sections for the absorption and emission of various particles (primarily neutrons, electrons, protons, and He nuclei). Some libraries include derived atomic displacement cross-sections that describe the effective number of displaced atoms arising from reactions with neutrons of a given energy. These displacement cross-sections are effective values obtained by combining all the possible reactions leading to displacements in collision cascades into a simple displacement cross-section following the method described by [Macfarlane et al., 1984]. Atomic displacement cross-sections can be found on various sites such as [for SPECTER, ENDF/B-V nuclear library, http://t2.lanl.gov/nis/data.shtml]. When two-stage transmutation reactions are important, as in the case of Ni-alloys [Greenwood, 1983; Greenwood and Garner; 1996; Griffiths et al., 2017], spectral averaged cross-sections are required. The code SPECTER generates spectral-averaged cross-sections for Ni [Greenwood and Smither, 1985].

The values for atomic displacement cross-sections from which one can calculate atomic displacement rates (by multiplying by the neutron flux) include the atomic displacements from all possible reactions occurring over the whole neutron energy range of a nuclear reactor. The LANL cross-sections do not address the fact that only a small fraction of point defects (1% - 10%) survive and are available to modify the microstructure. The survival fraction is a function of the cascade energy (i.e. the energy of

the primary knock-on or recoil atom). Low energy displacement cascades, e.g. those arising from (n,γ) reactions, have about twice as many point defects surviving the cascade as high energy displacement cascades. Although the MD simulations show that between 25% and 50% of the atoms displaced in a collision cascade survive spontaneous recombination, many of these form immobile clusters. It is estimated that only between 1% and 10% of the total displaced atoms are free to migrate to different sinks [Was, 2007]. The immobile clusters and the freely migrating point defects contribute to the microstructure evolution.

Irrespective of the processes by which displaced atoms and the corresponding vacancies are affective after being created in a displacement cascade, the property changes are often simply correlated with the initial calculated displacement damage. Work by [Jones et al., 2000] shows that best agreement with material property changes are obtained if an enhancement factor of 2 is applied for damage arising from neutrons with energies < 1 keV. This damage is achieved in practice by computing the full damage using the whole spectrum and then adding the damage created by the low energy neutrons (E < 1 keV) only.

There are typically about 4 or 5 atomic displacement arising from the recoil of γ emission. The (n,γ) reaction cross-section is only significant at low neutron energies and therefore only those neutrons with energies E < 1 keV need to be included in the damage efficiency correction. Compared with this effect, there are about 400-500 displacements occurring from fast neutrons (E > 0.1 MeV). As a rule-of-thumb therefore fast neutrons are 100 times more productive (per neutron) in creating atomic displacement damage compared with thermal neutrons (E < 0.5 eV).

In the case of Ni, neutron absorption of the main isotope (^{58}Ni) creates ^{59}Ni and this isotope can have a large effect on the irradiation damage production introducing a non-linearity to the damage production process. The ^{59}Ni evolves as a result of the reactions creating it and those that cause transmutation to other elements. The reaction cross-sections for ^{59}Ni are very high, especially at thermal neutron energies. Thus, ^{59}Ni will become important to irradiation damage production if there is any significant amount produced from ^{58}Ni, e.g. when the thermal neutron fluence exceeds 10^{25} n.m^{-2} (E < 0.5 eV).

At high temperatures in metal alloys bias-driven void swelling can result in significant strengthening, or embrittlement or both. Helium is an insoluble gas produced by (n,α) reactions in many engineering alloys. It promotes void swelling at high temperatures and, at low temperatures where vacancy mobility is low, results in the formation of a high density of bubbles (cavities). Low temperature He embrittlement is observed in Ni-alloys when the flux of He to grain boundaries is sufficiently high [Griffiths et al., 2013; Griffiths, 2017].

4.2 Irradiation Effects for Reactor Core Materials

The strength and ductility of irradiated materials is a function of both dpa, dpa rate, irradiation temperature and He concentration. Irradiation typically hardens a material while at the same time resulting in reduced ductility, Figure 4-1(a). The reduction in ductility often corresponds with a reduction in fracture toughness (energy absorbed prior to fracture) as expressed by the area under the stress-strain curve, Figure 4-1(b).

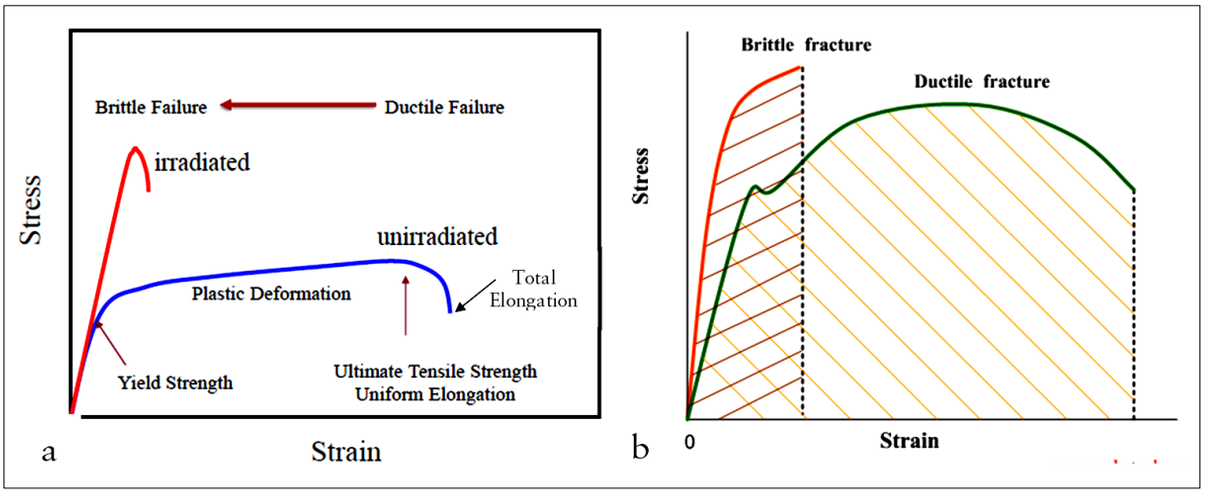

Figure 4-1: Irradiation hardening and loss of ductility of an irradiated metal. Schematic engineering stress-strain curves for irradiated and unirradiated material illustrating: (a) the various stages of deformation; (b) the effect of irradiation on fracture toughness (energy input to failure) that is given by the area under the curves.

4.2.1 Ferritic and Martensitic Steels

Ferritic steels are the most severely affected by low doses of irradiation. In the unirradiated state metals with a BCC crystal structure such as reactor pressure vessel (RPV) steels are prone to embrittlement, exhibiting a marked reduction in fracture energy at a critical temperature known as the ductile-brittle transition temperature (DBTT), Figure 4-2(a). For BCC metals the fracture mode shifts to cleavage at low temperatures resulting in de-bonding of the atoms on specific cleavage planes and a severe reduction in absorbed energy prior to fracture. This sharp drop in fracture energy with lower temperature is generally not exhibited by FCC and HCP metals with a close-packed crystal structure, Figure 4-2(b) [Jordan, 2016]. The main reason for this difference is that BCC metals are not close-packed and are more reliant on thermal activation for dislocation mobility compared with close-packed metals that exhibit easier slip at low temperatures. The likelihood of brittle fracture also increases at high strain rates because of the tendency for sluggish dislocation motion in BCC metals.

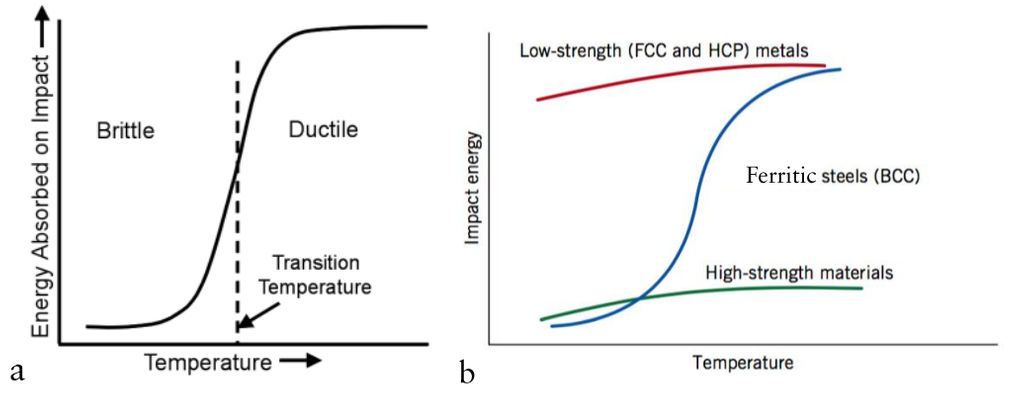

Figure 4-2: Impact energy as a function of temperature for different materials: (a) the ductile-brittle-transition-temperature (DBTT) that is characteristic of BCC metals such as ferritic stainless steels; (b) schematic diagram illustrating the difference between BCC and FCC or HCP metals that have close-packed crystal structures and do not exhibit a DBTT because they are more prone to dislocation slip and twinning.

Irradiation not only hardens BCC metals, it also results in a shift in the DBTT. The ductile-brittle transition can be represented as the point at which the yield stress and the fracture stress are the same,

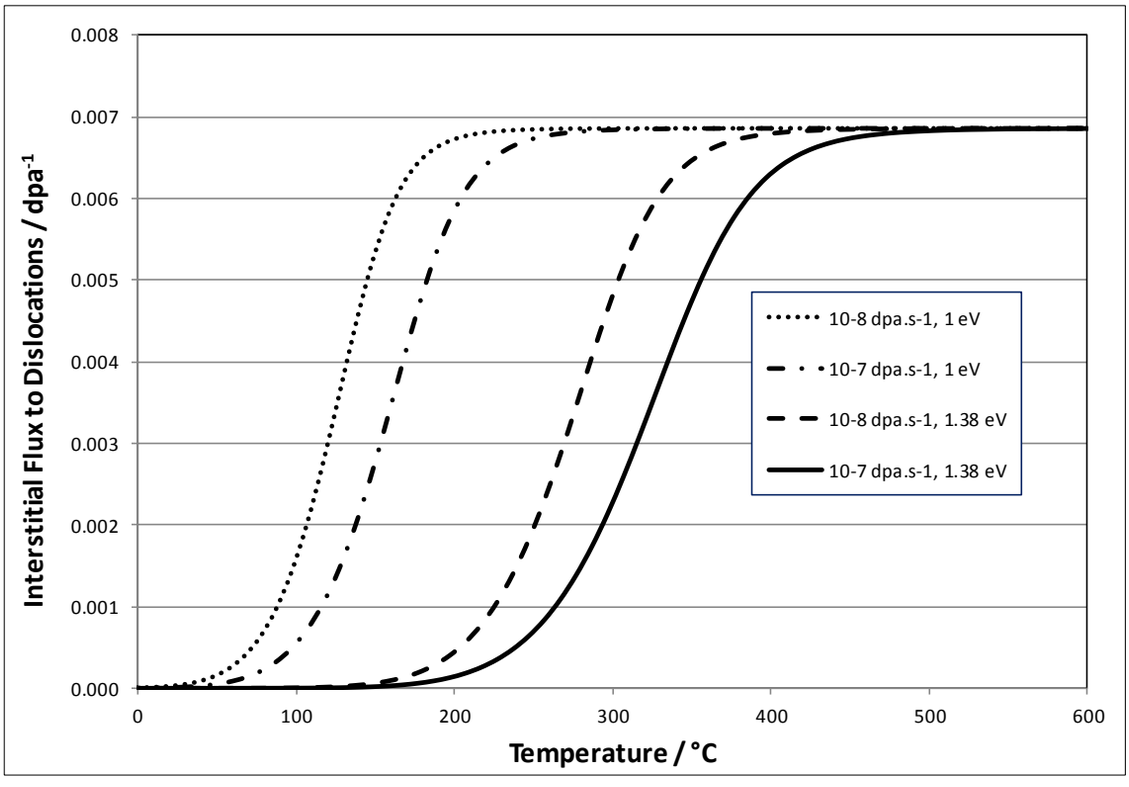

Figure 4-16: Rate theory output for interstitial flux to dislocations for a dislocation sink strength (density) = 10^{14} m^{-2} and an equal neutral sink strength. The dislocation bias for attracting interstitials = 30%. Nominal damage efficiency = 10% with two different rates for the production of freely migrating point defects.

4.2.3 Ni alloys

Ni-based alloys can be categorised into two classes: solution-annealed (SA), comprising a single face-centred-cubic austenitic phase, and aged or precipitation-harden-annealed (PHA), comprising ordered Ɣ' or Ɣ'' precipitates in an austenitic matrix. The response to neutron irradiation is markedly different. Mechanical test results from [Byun and Farrell, 2003] on SA and PH(A) materials irradiated in the HFIR reactor at 60 °C – 100 °C are summarised in Figure 2-67. At these low temperatures and doses up to 1.2 dpa the PH(A) material exhibits reduced ductility but little hardening with increasing dose, whereas the SA material exhibits marked irradiation-hardening in addition to a reduction in ductility.

The different response to irradiation is apparent at low doses because the PH material is already hardened prior to irradiation and further irradiation damage does not increase the strength appreciably. Additional changes are apparent at higher doses both because of He embrittlement and because of changes in the precipitate structure.

4.2.3.1 Solution-treated Ni-Alloys

Solution-treated Ni alloys are essentially similar to austenitic stainless steels in their response to irradiation. The alloys include the non-hardenable Inconel 600 and 690 but also includes solution-treated alloys such as Inconel 718 and X-750. The SA alloys have a response to low dose irradiation that is primarily dictated by the evolution of the dislocation loop structure.

Work by [Hunn et al., 2001] on H, He and 3.5 MeV Fe-ion irradiation of Inconel 718 at 200 °C showed that the solution-annealed Inconel 718 behaves similarly to 316 stainless steel over a large dose range. However, after an initial transient increase in hardness at low doses (< 1 dpa), softening of precipitation-hardened material occurred at increasingly higher doses. Softening (lower yield strength)

was exhibited by precipitation-hardened Inconel 718 at high doses (>10 dpa) but not for the same material in a solution-annealed state, Figure 2-68.

4.2.3.2 Precipitation-hardened Ni-Alloys

Precipitation-hardened alloys constitute a special case because the irradiation not only hardens the material, but also results in softening at high doses. The softening comes about because of the disordering and dissolution of the matrix precipitates.

The two main precipitation-hardened engineering alloys used in nuclear reactors are Inconel 718 and Inconel X-750. The Inconel 718 is hardened by $Ni_3(Ti,Al)$ Υ' and Ni_3Nb Υ'' precipitates and Inconel X-750 contains $Ni_3(Ti,Al)$ Υ' only. These precipitates increase the yield strength of these alloys making them ideal for use as spring materials. The effect of irradiation on ultimate tensile strength and yield strength is shown in Figure 2-69. After an initial increase in yield and tensile strength (from irradiation damage clustering) at low doses, these alloys exhibit a decrease in strength with extended irradiation exposure.

Prolonged irradiation in an environment producing both displacement damage and gas atoms (He and H) results in severe embrittlement similar to that observed for the V-15Cr-5Ti alloy (Figure 4-7 and Figure 4-8). Figure 2-70(a) shows stress-strain curves for Inconel 718 after irradiation in the LANSCE irradiation facility, which produces displacement damage as well as He and H, at temperatures between 367 °C and 400 °C. The He and H were not measured but are estimated to be between 2000 appm and 3000 appm at about 20 dpa [Griffiths, 2019]. The corresponding change in yield strength is shown in Figure 2-70(b) together with additional data for material irradiated at lower temperatures.

Similar data are observed for Inconel X-750. Figure 2-75 shows load-displacement curves for crush testing of spring material irradiated in a CANDU reactor and corresponding hardness data (a function of yield strength) as a function of dose. The data show that there is an initial increase in yield and ultimate tensile strength at low doses (6 dpa) followed thereafter by a reduction in strength and severe reduction in ductility similar to that exhibited by the V-15Cr-5Ti alloy (Figure 4-7) at higher doses. The reduction in strength and ductility has been attributed to the effect of He [Griffiths, 2019]. There is a decrease in hardness (yield strength) of the material at high doses, Figure 2-74. The He/dpa ratio is approximately 300 appm He/dpa.

The dependence of hardness (yield strength) on dose and temperature can be rationalised by the fact that at lower temperatures there is less evidence of cluster damage and more evidence of precipitate dissolution, Figure 2-78. Given that the cluster damage saturates at low doses, the long-term drop in yield strength at both high and low temperatures can be attributed to the dissolution of the γ' precipitates [Griffiths, 2014; Griffiths, 2019]. At power reactor operating temperatures, the irradiation damage clusters in the form of dislocation loops are generally low in density and small in size. The bright field TEM images in Figure 2-78 show that the dislocation structure is cleaner (fewer, or smaller, or both, point defect clusters) at the lower compared with higher irradiation temperatures. The insets show that there is more γ' dissolution at the lower temperature. One reason for the observation of fewer visible defect clusters at the lower temperatures is because of increased recombination [Griffiths et al., 2013; Griffiths, 2014; Griffiths, 2019].

The fracture surface of the unirradiated material has a ductile, dimple appearance but is brittle, intergranular for the irradiated material (Figure 4-17). The fracture surface of the irradiated sample is similar to that observed for the V-15Cr-5Ti alloy at high doses in Figure 4-8(a). The inter-granular fracture can be attributed to the accumulation of He-stabilised cavities on grain boundaries, which is a characteristic of He-embrittlement. Cavity accumulation on grain boundaries is observed in the Inconel X-750, Figure 4-18(a). Ion-irradiated alloys do not have voids decorating grain boundaries in the absence of He even though they may contain large numbers of voids, Figure 4-18(b). The stabilisation of cavities on grain boundaries is explained by the segregation of He for the neutron-irradiated material. There is no He for the ion-irradiated material and, in the absence of He, vacancies are simply absorbed at grain boundaries.

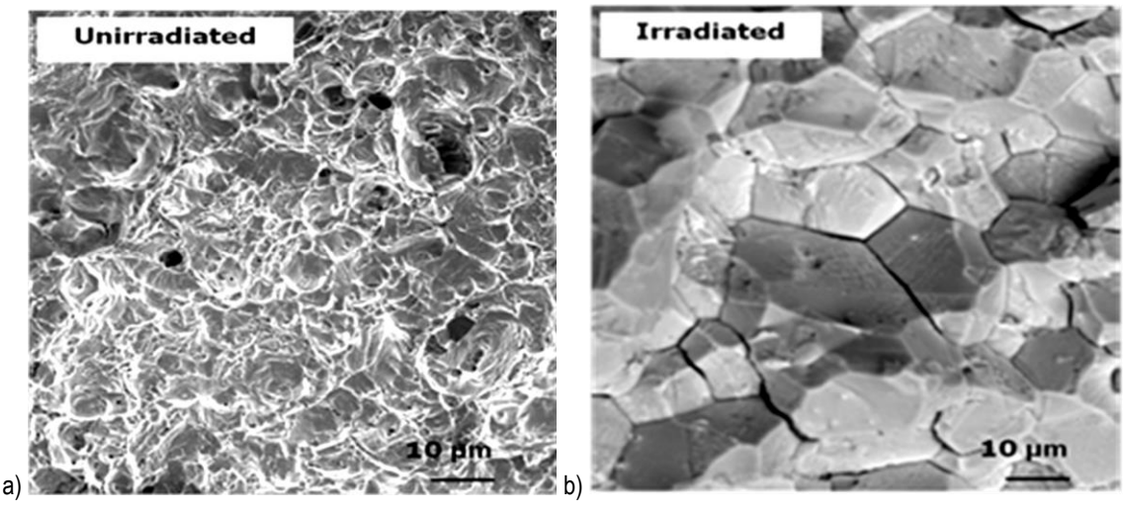

a) b)

Figure 4-17: Comparison of fracture surfaces for unirradiated and irradiated (to a dose of 23 dpa at >300 °C) Inconel X-750 after mechanical testing to breakage at room temperature. The unirradiated sample (a) exhibits ductile failure compared with the irradiated sample (b) that exhibits brittle inter-granular failure when tested at room temperature after irradiation [Griffiths, 2019].

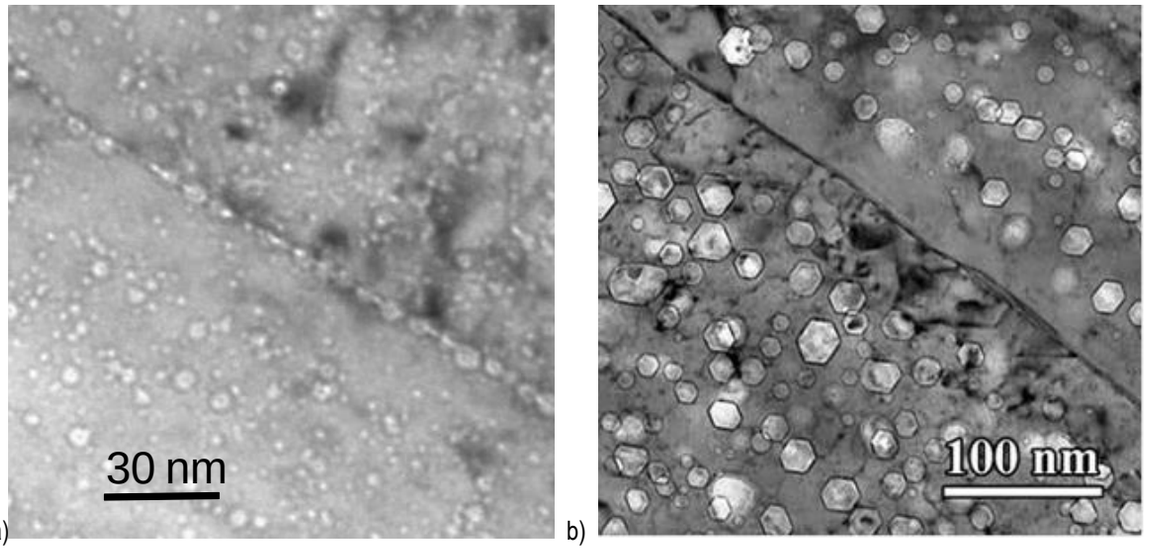

a) b)

Figure 4-18: (a) Cavity distribution on and near a grain boundary in Inconel X-750 irradiated in a CANDU reactor to a dose of about 60 dpa at about 300 °C; (b) Voids in an Fe-Cr-Ni alloy (MA957 after self-ion (Fe) irradiation to 500 dpa at 450 ˚C [Griffiths, 2019].

Whereas the softening of the Inconel X-750 can be attributed to the disordering and dissolution of the γ' precipitates, the embrittlement and loss of strength at high doses is attributed to the effect of He accumulating on grain boundaries.

For Inconel X-750 irradiated in a high thermal neutron environment such as exists in a CANDU reactor, not only does one see a decreasing yield strength with increasing dose but one also observes a *decrease* in ultimate tensile strength corresponding with the reduced ductility. Both the yield strength and the failure load can exhibit a negative trend with increasing neutron dose, and are a function of accumulated atomic displacement damage, or He production, or both. The changes in properties can be described schematically as shown in Figure 2-82.

Some materials exhibit low ductility (brittle or semi-brittle failure) because of fracture of, or at, secondary phases such as carbides on grain boundaries, or hydrides in the case of Zr-alloys. Hydrogen embrittlement can be important for ferritic steels, especially at low temperatures, but the mechanisms

are not well understood. Hydrogen is generally not deemed an issue for reactor components made from austenitic stainless steels and Ni-alloys operating at relatively high reactor temperatures (250 °C to 350 °C). According to Louthan et al. [Louthan et al., 1975], austenitic stainless steels "typically show only minimal susceptibility to adverse hydrogen effects" and "hydrogen-induced service failures of austenitic stainless-steel components are unlikely".

Even in the presence of embrittling elements such as hydrogen and carbon, irradiation is important by increasing the matrix strength so that the material can maintain higher stresses to be sustained without yielding thus shifting the failure to other parts of the microstructure, e.g. brittle second phases such as carbides and hydrides. These second phases, like He-stabilised cavities, often segregate at grain boundaries and the failure then appears inter-granular even though the grain boundary structure may remain intact, i.e. failure is not one of simple decohesion of the boundary.

4.3 Mechanisms and Microstructure

The change in mechanical properties during irradiation, whether yield strength, ultimate tensile strength or fracture toughness, are a function of the irradiation damage accrued. Historically, the dose for neutron irradiation has often been represented as fast fluence, i.e. accumulated neutron flux for energies, E > 1 MeV. Whereas such a measure is adequate for comparing doses for the same neutron spectrum it is not adequate when the spectra are significantly different [Mahmood et al., 2018]. Also, comparison with data from different irradiation sources (including ion irradiation) and the contributions to damage from sources other than neutrons (γ-photons for example) necessitates the use of a common parameter for measuring irradiation dose, in this case displacements per atom (dpa) where possible. When dpa data are not provided and the dose is represented as the accumulation of fast neutrons (E> 0.1, 0.82 or 1 MeV), conversion factors can be applied with some knowledge of the applicable neutron spectrum [Mahmood et al., 2018].

The change in mechanical properties is a function of the microstructure. The microstructure of the irradiated material is a function of the temperature, dose (dpa) and dose rate. Most discussions of the irradiation response of materials based on the microstructure evolution are based on qualitative assessments of the microstructure. Quantitative measurements of the microstructure are often difficult to obtain using traditional TEM observations and are subject to considerable errors. X-ray diffraction (XRD), however, can provided a robust measure of the microstructure. Although diffraction line-broadening analysis is subject to some interpretation the relative change in line-broadening is a good objective measure of the changes in microstructure, from dislocation loop evolution for example.

The effect of irradiation-induced microstructure on the yield strength of a material is often represented as the intrinsic effect of irradiation-induced precipitates and point defect clusters, each with a particular resistance to dislocation passage given by a strengthening factor (α) and the spacing of these barriers to slip in the slip plane (λ). The increment in yield strength is,

Equation 4-3:

$$\Delta\sigma_0 = \frac{\alpha}{\lambda} = \alpha\sqrt{(Nd)}$$

where N is the number density of impeding objects and d is their diameter [Was, 2007]. The strength factor (α) is also a function of the barrier diameter (d). Tan and Busby have developed a plot showing the effect of cluster size on strengthening factor, Figure 4-19.

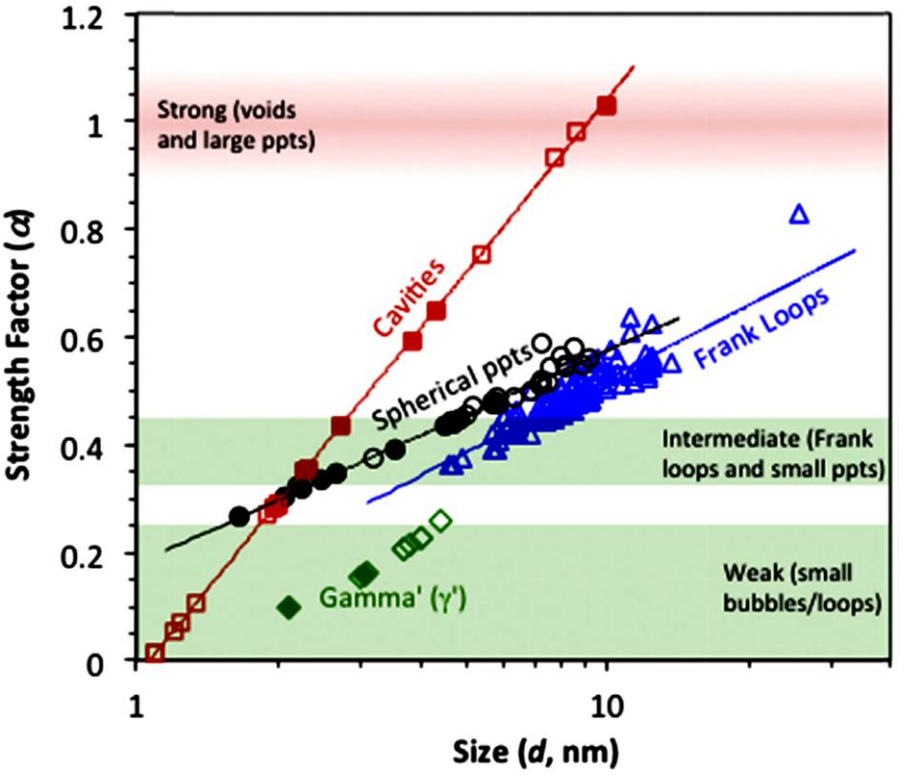

Figure 4-19: Calculated size-dependent strength factor at room temperature for spherical incoherent precipitates ppts (circles), coherent ppts (diamonds), Frank loops (triangles), and cavities (squares), [Tan and Busby, 2015].

The hardening effect can be regarded as simply an increase in the number of barriers to dislocation slip and is reflected to a large extent by the XRD line broadening. In the case of Zr-alloys the relationship between line-broadening and irradiation strength increment is shown for Zr-2.5 Nb pressure tubing in Figure 4-14(a). The UTS and ductility data (total elongation) are shown for samples irradiated in the OSIRIS reactor together with the XRD line-broadening (a measure of dislocation loop density). It is clear that there is a direct correlation between the dislocation density measured by XRD and the effect on UTS and ductility as one might expect.

Whereas cavities and precipitates impede dislocation motion by being barriers to slip, necessitation by-pass by either a cutting mechanism or a looping mechanism (Figure 2-65), dislocation loops impede the passage of slip dislocations by elastic interaction and junction formation. The simplest case with minimal impedance is when the gliding dislocation has the same Burgers' vector as the prismatic loop (see section 4.3). For all other reactions there are different types of junction formation and in some cases (the glide of a screw dislocation for example) where the prismatic loop cannot be consumed by the gliding dislocation and the by-pass mechanism is necessary for continued slip [Drouet et al., 2014].

4.4 Modelling the effects of irradiation damage on mechanical properties

The impressive progress in numerical calculation have opened the possibilities of running scientific computations that were not even conceivable a few decades ago. Without describing in detail all the techniques and results obtained for the different alloys of concern, the aim of this section is to present the general philosophy and examples of how the different scales between the atomic scale to the macroscopic behaviour are interlinked, in this new area of computational material science.

No details of the very complex computation procedures will be given, due to the very large number of techniques and their rapid evolutions (software selections, parameter adjustments, approximations for faster results and validities…) The aim of this section is only to give a feeling of what can be done and

6 Summary

In this report the possible methods for obtaining mechanical properties of irradiated materials are summarized. We describe tensile and fracture properties of four distinct structural materials used in nuclear reactors and provide examples of the varied response of these materials to residence in the reactors. Each basic element of the four materials has a different crystal structure: face-centred cubic – austenitic steel (γ-Fe) and nickel alloys (Ni); body-centred cubic- ferritic steel (α-Fe); hexagonal close packed – zirconium (α-Zr) alloys. Before residence in a reactor, each material exhibits smooth work-hardening either after gradual yielding or after a distinct yield point (α-Fe) followed by a maximum load leading to necking and rupture. Irradiation by neutrons either displaces atoms out of their position in the crystal lattice to form either vacancies or interstitial atoms, or transmutes some of the atoms to an isotope that eventually yields helium. The displaced atoms can aggregate to form dislocation loops that initially strengthen the lattice of all four materials; these loops can be annihilated by mobile dislocations in narrow bands and this process leads to local weakening, limited work-hardening and concomitant loss of plastic ductility. If the unirradiated alloy is strengthened by precipitation, this strengthening can be increased or reduced by irradiation as the precipitates are either formed (α-Fe, Ni- alloys) or dissolved (Ni-alloys). With sufficient helium, bubbles may form especially in grain boundaries and lead to embrittlement by intergranular fracture. If the unirradiated material fractures in a brittle manner by matrix cleavage at low temperature (α-Fe) or if the material contains a brittle phase that induces a general embrittlement (H in α-Zr), a transition to ductile behaviour at an elevated temperature can be postponed to a higher temperature after irradiation.

References

Adamson R. B. and Bell W. L., *Effects of Neutron Irradiation and Oxygen Content on the Microstructure and Mechanical Properties of Zircaloy*, Microstructure and Mechanical Behaviour of Materials, Proceedings: Int'l Symposiums, Xian, China, October, 1985, EMAS, pp. 237-246, Warley, UK, 1986.

Adamson R. B., Wisner, S. B., Tucker, R. P. and Rand. R. A., *Failure Strain for Irradiated Zircaloy Based on Subsized Specimen Testing and Analysis*, The Use of Small-Scale Specimens for Testing Irradiated Material, ASTM STP 888, W. R. Corwin and G. E. Lucas, Eds., American Society for Testing and Materials, 171-185, Philadelphia, 1986.

Adamson R. B, Garzarolli F., Patterson C., Rudling P. Strasser A. and Coleman K., ZIRAT15/IZNA10 Annual Report, ANT International, Mölnlycke, Sweden, 2010.

Adamson R, Coleman K, Mahmood S, Rudling P, ZIRAT18 STR on Mechanical Testing of Zirconium Alloys, Vol. I, Advanced Nuclear Technology International, Analysvägen 5, SE-435 33 Mölnlycke, Sweden, 2013a.

Adamson R, Coleman K, Mahmood S, Rudling P, ZIRAT18 STR on Mechanical Testing of Zirconium Alloys, Vol. II, Advanced Nuclear Technology International, Analysvägen 5, SE-435 33 Mölnlycke, Sweden, 2013b.

Adamson R.B., Coleman C.E. and Griffiths M., *Irradiation creep and growth of zirconium alloys: A critical review*, Journal of Nuclear Materials, Vol. 521, pp. 167-244, 2019.

Akhtar, A., *Basal slip in zirconium*, Acta Met., Vol. 21, pp.1-11, (1973).

Alam A. and Hellwig C., *Cladding Tube Deformation Test for Stress Reorientation of Hydrides*, Journal of ASTM International, Vol. 5, No. 2, Paper ID JAI101110, 2009.

Almirall, N. et al. *On the elevated temperature thermal stability of nanoscale Mn-Ni-Si precipitates formed at lower temperature in highly irradiated reactor pressure vessel steels.* Nature - Scientific Reports 9:9587, DOI: 10.1038/s41598-019-45944-z, 2019.

Almirall, N. et al. *Precipitation and hardening in irradiated low alloy steels with a wide range of Ni and Mn compositions*, Acta Materialia, Vol. 179, pp. 119-128, 2019.

Altstadt, E. *FP7 Project LONGLIFE: Overview of results and implications*, Nuclear Engineering and Design, Vol. 278, (2014) 753–757, 2014.

American Iron & Steel Institute (2002). High Temperature Characteristics of Stainless Steels, www.nickelinstitute.org/media/1699/high_temperaturecharacteristicsofstainlesssteel_9004_.pdf.

Andresen, P.L., and Was, G. S., "Irradiation Assisted Stress Corrosion Cracking", Volume 5, Comprehensive Nuclear Materials, Elsevier, Amsterdam, pp. 177-205, 2012.

Angeliu, T.M., Ward, J.T., and Witter, J.K., *Assessing the Effects of Radiation Damage on Ni-Base Alloys for the Prometheus Space Reactor System*, J. Nucl. Mater., Vol. 366, pp. 223-237, 2007.

Antolovich S. D., An Introduction to Fracture Mechanics, ASM Handbook – Fatigue and Fracture, Vol.19, pp. 371-380, 1997.

Arséne S. and Bai J. B., *A new approach to measuring transverse properties of structural tubing by a ring test*, Journal of Testing and Evaluation, JTEVA, Vol. 24, No. 6, pp. 386-391, 1996.

Asher, R.C. and Trowse, F.W., *The distribution of hydrogen in zirconium alloy fuel cladding: the effect of heat flux,* J. Nuclear Materials, Vol. 35, pp. 115-121, 1970.

ASME NB-2331, (1998) ASME Boiler and Pressure Vessel Code, Rules for Construction of Nuclear Power Plants, Division 1, Subsection NB 2331: Material for vessels.